Gcoupler: An AI-enhanced tool unveiled Endogenous Intracellular Allosteric Modulators of Evolutionary Conserved GPCR-Gα Interface

Sanjay Kumar Mohanty[1,†], Aayushi Mittal[1,†], Aakash Gaur[2,3], Saveena Solanki[1], Subhadeep Duari[1], Sakshi Arora[1], Suvendu Kumar[1], Vishakha Gautam[1], Nilesh Kumar Dixit[1], Karthika Subramanian[1], Tarini Shankar Ghosh[1], Debarka Sengupta[1,4], Shashi Kumar Gupta[2,3], Natarajan Arul Murugan[1], and Gaurav Ahuja[1,4]

[1]Department of Computational Biology, Indraprastha Institute of Information Technology-Delhi (IIIT-Delhi), Okhla, Phase III, New Delhi, 110020, India.

[2]Pharmacology Division, CSIR-Central Drug Research Institute, Lucknow, India

[3]Academy of Scientific and Innovative Research (AcSIR), Ghaziabad, India.

[4]Infosys Centre for AI, Indraprastha Institute of Information Technology-Delhi (IIIT-Delhi), Okhla, Phase III, New Delhi, 110020, India.

[†]Equal contributions

Correspondence: Gaurav Ahuja; Email: gaurav.ahuja@iiitd.ac.in.

Running title: Modulation of GPCR-Gα binding via intracellular metabolites

Keywords: apoptosis, Deep Learning, GPCR, hypertrophy, mating, yeast

ABSTRACT

Traditionally, the exogenous allosteric modulators of G protein-coupled receptors (GPCRs) have been extensively investigated due to their pharmacological significance. However, to date, only a handful of endogenous intracellular allosteric modulators are known, that too with inconclusive binding information and their associated phenotypes. This limitation primarily stems from the non-availability of robust computational techniques that entail unbiased cavity identification across GPCR protein topology, cavity-specific ligand design, their synthesis, and cross-validation. Here, we introduce Gcoupler, which leverages an integrative approach combining *de novo* ligand design, statistical methods, and Graph Neural Networks for rationally predicting high-affinity ligands. Gcoupler offers an efficient and comparatively faster route to explore allosteric sites of GPCRs, including the GPCR-Gα interface. We tested and validated the applicability of Gcoupler in decrypting the cellular metabolites that could intracellularly modulate the Ste2 (GPCR)-mediated pheromone-induced cell death in yeast. Our rigorous interrogation using Gcoupler and experimental approaches, including yeast genetic screening, RNA sequencing, high-resolution metabolomics, and functional assays, identified endogenous hydrophobic metabolites, mainly specific sterols, as intracellular allosteric modulators of Ste2p signaling. Elevated intracellular levels of these metabolites, either naturally, through genetic alterations, or exogenous treatment, rescue the pheromone-induced programmed cell death. Computational insights revealed that these metabolites harbor high binding affinity to the conserved GPCR-Gα interface and might trigger a cohesive response that potentially obstructs downstream signaling. Finally, by utilizing isoproterenol-induced, GPCR-mediated human and neonatal rat cardiac hypertrophy models, we observed that elevated metabolite levels attenuate hypertrophic response, reinforcing the functional and evolutionary relevance of this mechanism. In summary, our study reports a robust computational approach for efficiently exploring the allosteric sites in GPCRs.

INTRODUCTION

G Protein-Coupled Receptors (GPCRs) are among the most preferred drug targets due to their importance in regulating vital cellular functions such as homeostasis, growth, metabolism, and death [1–3]. Traditional therapeutic approaches devised to target GPCR activity are centered around the orthosteric or the ligand binding sites [4,5]. Recent advancements in the structural and functional information about the GPCRs led to identifying novel, albeit spatially distinct, allosteric sites that could modulate the receptor activity response [5–7]. These allosteric sites can be exploited using chemical probes to alter (positively or negatively) the GPCR-mediated physiological responses. While many exogenous synthetic compounds with allosteric characteristics are known in the literature, limited information is available about intracellular, allosteric, small molecule modulators, their mode of regulation, and their physiological relevance [8–13]. The practical design or identification of highly specific and high-affinity endogenous allosteric compounds demand efficient approaches leveraging structure-based drug design, artificial intelligence (AI), and biochemical assays, each possessing defined limitations. For example, classical computational SAR (structure-activity relationships) techniques demand a substantial amount of experimentally validated compounds for the designated cavity for predictive modeling, which, unfortunately, at least in the case of GPCRs, is the limiting factor [14,15]. Similarly, experimental approaches such as Förster resonance energy transfer (FRET), bioluminescence resonance energy transfer (BRET), and single-molecule detection fluorescence can be employed to validate potential allosteric compounds; however, their implementation for the hunt of novel intracellular allosteric modulators via high-throughput screening is technically challenging [16–18]. Identification and subsequent characterization of novel endogenous GPCR intracellular allosteric modulators harbor multiple challenges due to the lack of accurate topology information for multiple GPCRs [19], methods required to detect them, large-scale screening to evaluate their modulatory function, astronomically larger chemical space among others [1,20]. This necessitates the implementation of a hybrid computational approach that could leverage the power of the predictive structure approaches for unbiased detection of allosteric sites (cavities), *de novo* ligands synthesis based on cavity topological features, and finally, to accelerate the screening procedure, a helping hand from statistical methods and state-of-the-art deep learning approaches. While multiple computational tools have been developed over the years that allow *de novo* drug design, they largely lack practical suitability for discovering GPCR endogenous intracellular allosteric modulators due to computational constraints and excessive demand for domain knowledge and technical skills [21–27]. To overcome such limitations, we developed a Python package, Gcoupler, that leverages computational structural biology, statistical methods, and

deep learning approaches and offers a novel, computationally inexpensive, and highly efficient approach to decrypt the endogenous intracellular allosteric modulators of GPCRs systematically.

We demonstrated the usability and applicability of Gcoupler in identifying novel endogenous modulators of GPCRs by exploiting the α-pheromone (α-factor)-induced mating or programmed cell death pathway of *S. cerevisiae*. Ste2p (GPCR) is the hub protein of the yeast mating response, where the pheromone-bound Ste2p triggers the exchange of GDP for GTP in a heterotrimeric G protein (Gpa1p) and initiates mitogen-activated protein kinase (MAPK) signal transduction cascade, resulting in the expression of mating-related genes [28–30]. Notably, it has been previously reported that exposure to low doses of mating pheromones, either during the failed mating event or in the absence of a suitable partner, triggers programmed cell death (PCD) in the haploid cells [31–34]. Mechanistically, pheromone-induced PCD induction activates the Ste2/Ste3-mediated MAP-kinase signaling pathway, which triggers an increase in intracellular Ca^{2+} levels and mitochondrial activity, leading to the release of cytochrome c [31–34]. While the pheromone-induced PCD favors the diploid state, which is comparatively more advantageous than the haploid one, it is arguable that evolution only unilaterally supported one state over the other without imparting an innate defense mechanism to nullify accidental or intentional pheromone-induced PCD induction. Notably, it is well documented that the highly elevated, non-physiological levels of α-factor trigger PCD in less than half of the MATa population [33]. Moreover, an equivalent concentration of α-factor triggers distinct PCD kinetics across distinct laboratory strains; for example, BY4741 is more resistant than the W303 strain [35]. Earlier studies utilizing the genetic screening approach identified Yeast Suicidal Protein 1 (LAM1) and Yeast Suicidal Protein 2 (LAM2) as the positive regulators of α-factor-induced PCD [35]. While the exact mechanisms that facilitate resistive or sensitive response towards pheromone-induced PCD are still elusive, the evidence suggests the involvement of a previously undiscovered innate rescue mechanism that imparts resistance to MATa upon α-factor exposure.

We hypothesized that a subset of pheromone-resistant cells might regulate the Ste2p-mediated programmed cell death signaling via the endogenous intracellular metabolites by operating at the Ste2-Gα binding interface. Notably, recent single-cell RNA sequencing on yeast cells revealed the role of central metabolism in imparting cellular fitness towards adverse environmental challenges [36]. Using Gcoupler, we identified a subset of intracellular metabolites that could potentially bind to Ste2p (GPCR) at the Gpa1 (Gα) binding interface and obstruct the downstream signaling. Our computational results further suggest that hydrophobic ligands such as sterols strengthen the Gpa1p-Ste2p binding and might trigger a

cohesive response that potentially obstructs downstream signaling. Experimental evidence further supports these findings that the elevated intracellular levels of these metabolites rescue the pheromone-induced PCD. To evaluate the evolutionary conservation and possible clinically relevant translation of this mechanism, we tested these metabolites on human and rat isoproterenol-induced, GPCR-mediated cardiac hypertrophy model systems and observed attenuated response in the cardiomyocytes pretreated with GPCR-Gα-protein interface modulating metabolites. This study presents Gcoupler, a computational workflow as a Python package that leverages structure-based *de novo* ligand design and Graph-Neural Network-based identification of high-affinity ligands. Moreover, by leveraging Gcoupler, we underpinned the intracellular allosteric modulators (metabolites) and showed their functional importance in regulating α-factor induced PCD in yeast and isoproterenol-mediated hypertrophy models.

RESULTS

Structure-based ligand design and validation using Gcoupler

Identifying hit compounds for any given protein is a daunting task, primarily due to the diversity and complexity of the chemical space [20,37]. G-protein coupled receptors (GPCR) are one of the most pharmaceutically important targets because they regulate many essential human physiological functions, including growth, metabolism, and homeostasis [2,38,39]. Presently, computationally exhaustive *in-silico* methods (e.g., docking) or experimental approaches (e.g., protein structure-based methods) are used to identify and validate hit molecules. Both of these approaches are technically challenging and demand enhanced resources. Therefore, to ease and accelerate the ligand designing for distinct cavities on the topological surface of GPCRs, we developed the Gcoupler and provided it to the community as a Python Package or Docker image. Gcoupler adopts an integrative approach utilizing structure-based *de novo* ligand design, robust statistical method, and highly powerful Graph Neural Networks. It is primarily designed to identify ligands that could potentially bind to the GPCR-Gα-protein interface and modulate Gα-protein coupling, hence the downstream signaling.

The Gcoupler package possesses three significant modules, i.e., Synthesizer, Authenticator, and Generator, that collectively impart a smoother, user-friendly, and minimalistic experience for the end-to-end *de novo* ligand design. Due to the implementation of Graph Neural Network algorithm-based modeling approaches, Gcoupler provides a rapid solution for screening chemical libraries or user query compounds. Synthesizer, the first module of Gcoupler, takes a protein structure as input in PDB format and identifies putative cavities across the topological/entire protein surface. Gcoupler offers flexibility to the users to select either of its predicted cavities based on the users-supplied critical residues or by user-supplied cavity information (amino acids) using third-party softwares (e.g., Pocketome) [40] (refer Materials and Methods). Post cavity selection, the Synthesizer module allows structure-based *de novo* ligand designing to generate potential ligands and outputs the Simplified Molecular Input Line Entry System (SMILES) information of the synthesized compounds, three-dimensional cavity coordinates and other files required by the succeeding Gcoupler modules **(Figure 1a)**. The chemical composition of the *in-silico* synthesized ligands by the Synthesizer module is influenced by the cavity topology (3D) and its composition (pharmacophore). Noteworthy, the Synthesizer module of Gcoupler employs LigBuilder V3 [41], which utilizes the genetic algorithm (GA) for the *in-silico* ligand synthesis. Authenticator, the next module of Gcoupler, further segregates the synthesized compounds into high-

affinity binders (HAB) and low-affinity binders (LAB) by leveraging a structure-based virtual screening approach (AutoDock Vina) and statistically-backed hypothesis testing for distribution comparisons **(Figure 1a)**. The Authenticator module outputs the free binding energies of all the generated compounds. The statistical submodule further segregates the compounds into HAB and LAB while ensuring the optimal binding energy threshold and class balance. Of note, Authenticator leverages the Empirical Cumulative Distribution Function (ECDF) for binding energy distribution comparisons of HABs and LABs and performs Kolmogorov–Smirnov test [42], Epps-Singleton test [43], and Anderson-Darling Test [44] for hypothesis testing. Moreover, it also follows a strict criterion to ensure adequate representation of HABs and LABs to avoid class imbalance issues for the downstream analysis. Importantly, in case the Authenticator module fails to generate optimal LABs, Gcoupler offers flexibility to users to either use the inbuilt function to generate decoys or supply decoys generated using third-party softwares. Moreover, it allows users to supply negative class datasets of their choice based on domain knowledge [45]. Generator, the last module of the Gcoupler, takes these outputs and applies state-of-the-art Graph Neural Network algorithms such as Graph Convolution Model, Graph Convolution Network, Attentive FP, and Graph Attention Network to generate classification models [46]. The Generator submodule has pre-automated implementation of the hyperparameter tuning and cross-validation. By default, Gcoupler builds four distinct base models using the aforementioned algorithms. Moreover, it also supports the augmentation of the best base model performance metrics by facilitating hyperparameter tuning and parameter cross-validation (default: three folds). Finally, it allows users to predict the binding probability of user-supplied query compounds **(Figure 1a)**. For the post-model data analysis, Gcoupler offers two different algorithms, i.e., G-means and Youden's J statistics, which further facilitate users in determining the optimal probability threshold to narrow down on high-confidence hit compounds **(Supplementary Figure 1b)**. Together, Gcoupler overcomes the previously mentioned prerequisite limitations and offers a hassle-free and highly efficient method that leverages *de novo* ligand design and deep learning algorithms.

To test the performance of the Gcoupler, we performed rigorous benchmarking with five different GPCRs (AA2AR, ADRB1, ADRB2, CXCR4, and DRD3) with their experimentally elucidated active ligands and their number-matched decoys [45]. Notably, the Synthesizer module of Gcoupler accurately identified the reported orthosteric ligand-binding site for all five GPCRs, further validating the robustness of the implemented *de novo* cavity identification algorithm **(Figure 1b)**. For each of these cavities (one per GPCR), we next built classification models using the Generator module of Gcoupler using the default parameters and selected the best-performing model for the downstream analysis **(Supplementary**

Figure 2a-b). Finally, the projection of known active compounds and their decoys for the respective GPCRs on the models revealed the acceptable performance of the Gcoupler workflow in segregating True Positives (active ligands) and True Negatives (decoys) **(Figure 1c, Supplementary Figure 2c)**. Furthermore, we also validated Gcoupler in identifying the allosteric sites and their ligands using the experimentally validated GPCR-ligand complexes from the PDB databank. For this, we selected three GPCR-ligand complexes (β2AR-Cmpd-15PA, CCR2-CCR2-RA-[R], and CCR9-Vercirnon) recently summarized by Shen and colleagues [47]. We next removed the ligands from the PDBs and performed the standard Gcoupler workflow using the default parameters. Notably, similar to the orthosteric site (discussed above), Gcoupler accurately identified the allosteric ligand binding sites for all three GPCRs **(Supplementary Figure 2d)**. Evaluation of the performance metrics of the generated classification models for each GPCR revealed acceptable performances, with the AUC-ROC values above 0.95 across all cases **(Supplementary Figure 2e-f)**. Projection of the experimentally validated ligands on their respective models revealed their accurate classification by Gcoupler **(Supplementary Figure 2g)**. Finally, we compared the run time of the Gcoupler with a state-of-the-art molecular docking algorithm (AutoDock) [48], for which we selected the alpha-1A adrenergic receptor (ADRA1A) **(Supplementary Figure 1a, c)**. We selected this receptor due to the availability of the comparatively large number of reported experimentally validated agonists in the ChEMBL31 database [49]. For better comparison, we followed the conventional steps of AutoDock Tools for molecular docking while keeping track of execution time for each step during the whole process till completion **(Supplementary Figure 1a, d)**. We also followed the same timestamp procedure for the Gcoupler, including its separate module sub-functions **(Supplementary Figure 1a, e)**. The processing time consumption comparison between the two approaches revealed that Gcoupler takes 13.5 folds less time than AutoDock (**Supplementary Figure 1f)**. It is worth noting that AutoDock Vina might be one of the confounding factors for this observed accelerated speed, in addition to the ML/DL implementation [50–52]. Both approaches produced similar predictions of the experimentally validated active compounds, i.e., low binding energy and high predicted probability for all the 993 known agonists **(Supplementary Figure 1g-i)**. These results suggest that Gcoupler offers a novel and highly rapid alternative approach to ligand design.

To gain deeper insights into the GPCR-Gα-protein interface from the sequence, structural, and functional perspectives and to investigate whether the intracellular metabolites could target the exposed, intracellular GPCR-Gα-protein binding interface, we first downloaded all the experimentally deduced structures of the human GPCR-Gα complexes and systematically investigated and extracted the GPCR-Gα interacting interface residues **(Figure 1d, Supplementary Table 1)**. Next, by interrogating the sequence level amino acid

conservation at the GPCR-Gα-protein interface, we identified multiple conserved motifs, including the canonical DRY, CWxL, and NPxxY motifs [3] **(Figure 1e)**. To determine the topological similarity of the GPCR-Gα-protein interface, we identified and extracted the cavities across all GPCR-Gα-protein complexes and observed structural conservation as indicated by normalized Root Mean Square Deviation (RMSD) values (mean: 1.47 Å; median: 0.86 Å) **(Figure 1f-h, Supplementary Figure 2h-i, Supplementary Table 2)**. Finally, to test whether this topological and sequence conservation also impacts the ligand profiles that could potentially bind to this interface, we performed the Gcoupler workflow on all 66 GPCRs and synthesized ~50 unique ligands per GPCR **(Figure 1f).** We next computed and compared the physicochemical properties (calculated using Mordred) of these synthesized ligands and observed higher cosine similarity, indicating functional conservation of the ligand profiles that could bind to these interfaces **(Figure 1f, i)**. In summary, we used Gcoupler to systematically evaluate and analyze the ligand profiles of the GPCR-Gα-protein interface and observed a higher degree of sequence, topological, and functional conservation.

Gcoupler reveals endogenous, intracellular Ste2p allosteric modulators.

Next, we used Gcoupler to investigate the α-factor-mediated programmed cell death/apoptosis in yeast to identify novel (hitherto uncharacterized) intracellular allosteric modulating metabolites that impart natural resistance to PCD induction. The yeast mating pathway is one of the most extensively studied cellular pathways to date [28,29,33,34]. To delineate the identity and mode-of-action of endogenous metabolites that might modulate the GPCR-G-protein interface, we used the yeast mating receptor Ste2p, a pheromone-activated G protein-coupled receptor, as a model system. Importantly, our central aim is to pin down the intracellular metabolites that can bind to the Ste2p-Gpa1p interface and modulate the signaling cascade **(Figure 2a)**. To achieve this, we used Gcoupler to screen for such metabolites against the Yeast Metabolome Database (YMDB) [53]. We utilized the recently elucidated cryo-EM structure of the Ste2 protein [54] and performed a small-scale molecular dynamic simulation by using a yeast phospholipid composition-based lipid bilayer environment [55], and subjected the simulated stable structure to the Gcoupler workflow **(Figure 2b, Supplementary Figure 3a-g)**. The Synthesizer module of the Gcoupler package identified 17 potential surface cavities spanned across the extracellular, intracellular, and transmembrane regions of the Ste2 protein surface **(Figure 2c, Supplementary Figure 3h-k)**. Careful interrogation of the structurally-supported Ste2p-Gpa1p interface revealed two distinct predicted cavities (annotated as IC4 (Intracellular Cavity 4) and IC5 (Intracellular Cavity 5)), collectively capturing >95% of the interface

regions **(Figure 2d, Supplementary Figure 3l, m)**. We also measured the residue level conservation of the Ste2 protein by leveraging Ste2 protein sequences from 14 other closely related yeast species. Residue level conservation scores revealed higher conservation across IC4 and IC5 **(Supplementary Figure 3l, m)**. We next synthesized ~500 *in-silico* synthetic compounds for both IC4 and IC5 each by leveraging the Synthesizer module of Gcoupler.

To test whether the chemical space of the *in-silico* synthesized ligands is cavity-specific, we performed a stringent evaluation by comparing the chemical heterogeneity of the 100 synthesized ligands, each from IC4 and IC5, with an extracellular cavity (EC1). Of note, EC1 does not harbor any overlapping residue with IC4 or IC5 and possesses distinct pharmacophore properties **(Supplementary Figure 4a, d-e)**. We next computed the atom pair fingerprints and visualized the chemical heterogeneity in the low dimensional space using 2D and 3D PCA **(Supplementary Figure 4b-c)**. These results suggest that the Synthesizer module of Gcoupler generated cavity-specific ligands by leveraging both the cavity topology (3D) and its composition (pharmacophore). Furthermore, we also evaluated the reproducibility of the Gcoupler runs by selecting the IC4 cavity of the Ste2p and generated 100 *in-silico* compounds per run using the Synthesizer module of the Gcoupler workflow. Visualization of the chemical heterogeneity between the compounds generated via different runs in the low dimensional space using 2D/3D PCA and pairwise Tanimoto Similarity using atom pair fingerprints suggest heterogeneous and overlapping chemical composition among the synthesized ligands across all five runs **(Supplementary Figure 4f-h)**. Post these performance/reproducibility checks of Gcoupler; we finally segregated the 500 *in-silico* synthesized ligands for IC4 and IC5, each into high-affinity binders (HABs) and low-affinity binders (LABs) by the Authenticator module of Gcoupler. Notably, the estimated binding energy threshold was set at -7 kcal/mol, a widely accepted cutoff in virtual screening **(Figure 2e,f)**. A deep investigation into these classified synthetic compounds showed a comparable similarity between the HABs and LABs of the aforementioned target cavities, respectively **(Supplementary Figure 3n, Supplementary Figure 5a-b, Supplementary Table 3)**. Finally, the Generator module built classification models by implementing four distinct Graph Neural Network algorithms. Comparing the model performance metrics suggests that Attentive FP outperformed other algorithms for both cavities **(Figure 2g, Supplementary Figure 5c)**. Finally, we screened yeast metabolites, compiled from YMDB, on the best-performing model (hyperparameter tuned Attentive FP model) and predicted metabolites that could potentially bind to the IC4 and IC5 of the Ste2p-Gpa1p interface with a binding probability cutoff of > 0.5 **(Figure 2e)**. To further optimize the lead metabolite list, we parallelly performed the standard molecular docking using AutoDock with YMDB

metabolites against IC4 and IC5 of Ste2p, respectively, and finally selected the consensus metabolites (binding energy < -7 kcal/mol and binding probability > 0.5) for the downstream analysis **(Figure 2e, Supplementary Figure 3o, Supplementary Table 4)**. Of note, the consensus metabolites list was further segregated into HAM (High-Affinity Metabolites) and LAM (Low-Affinity Metabolites) based on the binding prediction probability (cutoff = 0.5). Comparative analysis of the binding prediction probabilities of Gcoupler and binding energies from Autodock of HAB and LAB revealed a significant negative correlation that further validates our novel approach's authenticity **(Figure 2h).** Of note, as expected, HAMs and LAMs possess distinct atomic fingerprints, as indicated by the Principal Component Analysis **(Supplementary Figure 5d)**. Furthermore, the functional group enrichment analysis of these metabolites suggests enrichment of R2NH, R3N, ROPO3, ROH, and ROR functional groups in the high-affinity binding metabolites for both cavities **(Figure 2i, Supplementary Figure 5e)**. Finally, to gain the pathway-level information about these putative endogenous intracellular allosteric modulators of Ste2p, we performed Pathway level Over Representation Analysis (ORA)[56] and observed the selective enrichment of metabolites involved in the steroid, sesquiterpenoid and triterpenoid biosynthesis and one carbon pool by folate pathways **(Figure 2j)**.

To further gain confidence in the obtained potential allosteric modulators via Gcoupler, we performed rigorous control analyses where we evaluated the performances of the Authenticator and Generator modules and also performed blind docking with the YMDB metabolites on Ste2p. In the former case, we removed the class information (HAB and LAB labels) from the *in-silico* compounds synthesized for the IC4 cavity of the Ste2p, which resulted in a heterogeneous pool of chemical compounds. We next randomly split the training and testing data (5 iterations) and build independent models. Our results suggest that compared to the Authenticator-guided data splitting (HAB and LAB), the random splitting resulted in poor model performances **(Supplementary Figure 4i)**, suggesting the robustness of the Authenticator module. Additionally, we also evaluated the impact of the size of the training data on the model performance. To achieve this, we randomly selected 25%, 50%, 75%, and 100% of the *in-silico* synthesized compounds of the Ste2p IC4 cavity and built models using default parameters. We evaluated the model performance by projecting a subset of metabolites from the YMDB database (Version 2.0). Our results revealed a significant increase in the model performance with increased training data size **(Supplementary Figure 5f-g)**. For the latter case, we performed blind docking by AutoDock for the Ste2p with the YMDB metabolites and compared these results with the cavity-specific Docking via AutoDock and Gcoupler predictions. As expected, in contrast to the cavity-specific Gcoupler and AutoDock, where we observed significant segregation of the HAM and

LAM at -7 kcal/mol Binding Energy (BE) cutoff and 0.5 as the probability cutoff of Gcoupler, we failed to observe any striking differences for the HAM **(Supplementary Figure 5h)**. Taken together, by using Gcoupler, we narrowed down cellular metabolites that could potentially bind to the Ste2p-Gpa1p interface and modulate pheromone-induced PCD or mating response.

Ste2p-Gpa1p interface regulatory metabolites inhibit pheromone signaling.

Gcoupler revealed a subset of intracellular metabolites that could potentially bind to the Ste2p-Gpa1p interface and regulate the downstream signaling. To test the impact of these metabolites on the Ste2-mediated signaling cascade, we performed a genetic screening of the metabolic mutants. We first mapped the predicted allosteric-modulating metabolites to the biochemical pathway space using KEGG [57] and MetaCyc [58] and identified the enzymes responsible for processing these metabolites **(Figure 3a,b, Supplementary Table 5)**. Notably, these databases constitute comprehensive repositories of biological pathway information, encompassing molecular interactions and metabolic networks, facilitating advanced computational analysis. Among the 53 single metabolic mutants (+ *ste2Δ*) used for screening, only Ste2 was reported in the KEGG pathway (ID: sce04011) for an altered mating response **(Supplementary Figure 6a)**. Second, we performed the large-scale activity screening of single metabolic mutants, assuming that their loss leads to the intracellular accumulation of these selected metabolites and, therefore, be used as a proxy to evaluate the crosstalk between metabolism (metabolites) and GPCR modulation **(Figure 3a)**. The signaling cascade activity was estimated using the α-factor-induced PCD assay using Propidium Iodide (PI). Briefly, selected single metabolic mutants (MATa) were grown under optimal growth conditions until the late log phase (16 hours). Noteworthily, intercomparison of the growth profiles of these single metabolic mutants revealed varied growth responses with respect to the wild-type, with the majority of the mutants harboring delayed growth response **(Supplementary Figure 6b)**. The late log phase cells were treated with the α-factor, and the PCD induction was measured using the PI-based cell viability assay **(Figure 3c)**. Heat-killed cells were used as the positive control (100% cell death). As expected, we observed a significant increase in the PI fluorescence in the wild-type BY4741 yeast strains treated with α-factor, indicating pheromone-induced PCD, whereas no significant death was observed in the *STE2* loss of function mutants. Interestingly, most single metabolic mutants (94.4%) resisted the α-factor-induced cell death, while a subset of them also displayed accelerated growth in the presence of α-factor, indicating a cross-talk between the central metabolism (or metabolites) and the Ste2 signaling. Our screening procedure also revealed some metabolic mutants that harbor enhanced sensitivity to the α-

factor **(Figure 3d)**. These results indicate that a significant proportion of Gcoupler-predicted metabolites could directly or indirectly influence the Ste2 signaling pathway, establishing a link between metabolism and Ste2 signaling.

We next performed a high-resolution metabolomics approach to gain further insight into the metabolic pathways or metabolomes imparting α-factor-induced PCD resistance. To achieve this, we first selectively enriched the cells that tolerated the α-factor-induced PCD at different pheromone concentrations, termed as survivors **(Supplementary Figure 6c)**, and subsequently performed high-resolution metabolomics to uncover their metabolic profiles **(Figure 3e)**. Of note, we exposed yeast cells to the increasing concentrations of α-factor to narrow down on differentially enriched metabolites in the surviving population. In addition to the wild type, we profiled the Ste2 knockout. Unbiased high-resolution metabolome analysis revealed a subset of metabolites differentially and significantly enriched in the survived population **(Figure 3f, Supplementary Figure 6d-f, Supplementary Table 6)**. In a cross-comparison analysis, we observed an overlap of seven metabolites between the Gcoupler prediction of Ste2p intracellular allosteric modulators and differentially-enriched metabolites from the survived cells, and among these, Ubiquinone 6 and Zymosterol showed prominent enrichment in the survived cells at all tested concentrations **(Figure 3g-i, Supplementary Figure 6g)**. Moreover, Over-Representation Analysis (ORA) of the differentially-enriched metabolites suggests their involvement in glyoxylate and dicarboxylate metabolism, purine metabolism, vitamin B6 metabolism, etc. **(Supplementary Figure 6h)**. Taken together, the results from genetic screening of the metabolic mutants and untargeted metabolomics from the PCD-survived mutants hint towards the interplay between the central metabolism and Ste2 signaling. Notably, these experimental results also pinpointed two key computationally-predicted metabolites that could potentially impart resistance against α-factor-induced PCD.

Elevated metabolic levels selectively inhibit GPCR signaling.

We next asked whether the observed resistance toward α-factor-induced PCD in single metabolic mutants might be the direct consequence of the identified metabolites or a pleiotropic response due to an altered genome. To answer this, we exogenously elevated zymosterol (ZST), ubiquinone 6 (CoQ6), and lanosterol (LST) levels in the wild-type strain and measured α-factor-induced PCD by three different techniques. Notably, all these three metabolites were predicted as a high-affinity binder to the Ste2p-Gpa1p interface by Gcoupler (prediction probability > 0.99) and were also supported by the docking technique; however, lanosterol (LST) alone was not detected in our untargeted metabolomics screening. Methodologically, we first pre-loaded the yeast cells with these metabolites for 24

hours. Notably, in almost all the cases, except for 10 μM concentration of lanosterol, we did not observe any significant alterations in the yeast growth profiles, indicating the physiological relevance of the selected doses **(Supplementary Figure 7a)**. Post-loading the cells with metabolites, they were screened for alterations in the α-factor-induced PCD induction by measuring their growth profiles, cellular viability measurement using PI, and cellular viability and vitality measurement using FUN™1 staining [59,60]. Regarding growth kinetics-based PCD screening, we measured and compared the area under the growth profile's curve (refer to methods section). As expected, we observed a significant decrease in AUC values in the wild-type strain treated with α-factor, while no significant differences were observed in the metabolite pre-loaded cells as well as in the *ste2Δ*, indicating the role of these metabolites in modulating Ste2p signaling **(Figure 4a, Supplementary Figure 7b)**. A similar rescue phenotype was observed in the pre-loaded cells using the PI-based fluorometric measurement for cell viability. In this case, heat-killed cells were used as a positive control **(Figure 4b, c, Supplementary Figure 7c)**. Finally, we used FUN™ 1 staining to estimate and compare the cell vitality and viability using fluorescent microscopy. In the case of the FUN™ 1-based assay [59], we used acetic acid, an alternative exogenous stimulus, to induce PCD in yeast [61,62]. The quantification of metabolically active and viable (faint green with red spots) cells revealed α-factor-induced PCD rescue response in the case of cells pre-loaded with zymosterol (ZST), ubiquinone 6 (CoQ6), and lanosterol (LST) compared to the non-pre-loaded wild-type cells. As expected, we did not observe α-factor-induced PCD in the *ste2Δ* cells. Interestingly, the observed PCD rescue response in the metabolite-pre-loaded cells was only valid for α-factor but not in the acetic acid treatment **(Figure 4d, e)**. These results suggest that the observed rescue response is exclusive to α-factor-induced PCD (and not a consequence of an altered response) and likely via modulation of the Ste2p-Gpa1p interface.

Next, we probed whether the observed modulation of Ste2 signaling only applies to the exogenous pheromone exposure-based assays (as discussed above) or if it also modulates the natural yeast mating behavior, an alternate but natural proxy to evaluate the Ste2 signaling pathway [63]. We investigated this by performing a mating assay with MATa and MATα strains. Of note, we used *ste2Δ* strain (MATa) as a negative control in the mating assay [64]. In line with the aforementioned exogenous pheromone exposure-based assays, the mating assay also revealed a decline in Ste2 signaling in metabolite-pre-loaded cells, suggesting the interlink between these metabolites and Ste2p signaling. Notably, in the case of ubiquinone 6 (CoQ6), we failed to observe any significant decline in the mating response **(Figure 4f, Supplementary Figure 7d),** which might be due to the naturally lower levels of

α-factor in contrast to the artificially elevated conditions used for cellular pre-loading in the aforementioned assays.

We next investigated whether the interaction of these metabolites at the Ste2p-Gpa1p interface is stable or transient. To achieve this, we performed three independent replicates of molecular dynamics (MD) simulations (short run of 100 ns) of the Ste2p-metabolite complex for both cavities **(Figure 4g-i, Supplementary Figure 8a)**. MD simulation results suggest that the interactions between the metabolites and Ste2p at the Ste2p-Gpa1p interface are thermodynamically stable in almost all the cases across both the cavities (IC4 and IC5), except for the ubiquinone 6 (CoQ6), which harbored a fluctuating Root Mean Square Deviation (RMSD) over simulation timeframe **(Figure 4i)**. Notably, fluctuating RMSD is observed only in the case of IC5, while it is within the permissive range for IC4 **(Figure 4i, Supplementary Figure 8b)**. We further evaluated IC4 by performing a longer simulation run for 550 ns with these three Ste2p-metabolite complexes and observed stable complexes in the case of zymosterol (ZST) and lanosterol (LST) while observing fluctuations in the ligand RMSD for ubiquinone 6 (CoQ6) post 100 ns **(Supplementary Figure 9a)**. To gain further insight into the contributing residues from the MD simulations, we performed a residue-wise decomposition analysis that provides information about the energy contributions from the different residues to total binding free energies **(Supplementary Figure 8c)**. These results suggest that IC4 and IC5 specific residues predominantly contribute to the total binding free energies. Notably, the binding free energies are obtained as an average of over 500 configurations corresponding to the last 50 ns of the MD simulations. Collectively, these simulation results could potentially explain the non-significant defects in the mating efficiency of the MATa pre-loaded with ubiquinone 6 (CoQ6) **(Figure 4f)**.

Attenuation of GPCR-mediated Hypertrophy Response by Intracellular Allosteric Modulators

To gain deeper insight into the mode of action of these metabolites in inhibiting Ste2p signaling, we first analyzed their impact at the orthosteric site, i.e., α-factor binding. We performed protein-peptide docking of Ste2p and α-factor and observed that metabolite-binding at the Ste2p-Gpa1p interface favors the α-factor interaction, as inferred from the binding free energies ΔG (kcal/mol) **(Supplementary Figure 9b-c)**. We also analyzed protein-protein interaction between the Ste2p (GPCR) and miniGpa1-protein[54] by selecting GPCR configurations with and without metabolite-induced altered cavity topologies (IC4 and IC5), respectively (frames output from the aforementioned Ste2p-metabolite complex simulations) and computed the dissociation constant (K_d), binding affinity (ΔG) and the

structural changes in the overall Ste2p topology **(Figure 5a-b, Supplementary Figure 9c-d)**. These computational analyses revealed that in contrast to metabolite-free Ste2p-Gpa1p interaction, referred to as wild-type (WT) condition, the K_d value is multi-fold lower in the presence of metabolite, indicating a cohesive response induced by these metabolites **(Figure 5a-b)**. A multi-fold lower K_d value further indicates and potentially explains that the metabolites binding favors Ste2p (GPCR) and miniGpa1-protein interaction and enables the establishment of a stable complex that might influence the shielding of the effector-regulating domains of the Gpa1p or influence its binding with the Ste4p (Gβ)-Ste18p (Gγ) complex. To gain a deeper understanding, we next asked whether hindering the metabolite binding at the Ste2p could reverse the Ste2p-Gpa1p interaction dynamics. Due to the overlap between the metabolite interacting residues and the Gpa1 binding site, the site-directed mutagenesis may not provide a feasible solution as it might attenuate the Gpa1 binding and could entirely inhibit the downstream signaling, mimicking the Gpa1 loss of function mutant phenotype. Thus, mutants obtained using this approach could not be used to evaluate the desired metabolites-induced rescue phenotypes. To overcome these limitations, we performed *in-silico* screening, where we computationally generated site-directed mutants of Ste2p to alter metabolite binding and performed docking with Gpa1p **(Figure 5c)**. Our results indicate that alterations in the metabolite-binding residues trigger a multi-fold increase in the dissociation coefficient of the Ste2p-Gpa1p complex, suggesting loose interaction **(Figure 5d, Supplementary Figure 9e)**. Notably, the observed effect is contrary to the one induced by metabolite binding to the wild-type Ste2p, further strengthening the observed working model, i.e., metabolite-binding at the Ste2p-Gpa1p interface facilitates the formation of the stable complex (lower K_d values), and therefore, explains the loss of downstream signaling **(Figure 5b, d)**.

We next performed RNA-sequencing analysis to gain an unbiased view of the mode of action of these metabolites in attenuating Ste2p (GPCR)-mediated pheromone-induced cell death in yeast **(Figure 5e)**. Notably, we selected LST (metabolite) for this analysis due to its robust rescue response in all tested assays. Like the cellular assays discussed above, we pre-loaded the cells with and without LST, treated them with the α-factor, and analyzed their transcriptomes **(Figure 5e)**. Transcriptomics analysis of the wild-type (untreated with metabolites; referred to as control) cells with and without α-factor revealed significant expression changes in the genes related to critical cellular processes **(Figure 5f; left panel, Supplementary Figure 9f; upper panel)**. Of note, careful examination of the differentially expressed genes identified multiple genes previously characterized to be involved in regulating cellular apoptosis or mating responses in yeast **(Figure 5g)**. Interestingly, two of the differentially expressed genes (*GSY1* and *PPT2*) **(Supplementary Figure 9f; upper**

right panel) are linked to the accumulation of hit metabolites **(Figure 2j)** and showed a resistive cell death response towards α-factor treatment **(Figure 3c-d)**. Notably, since the α-factor exposure duration allows the enrichment of the survived population, it indicates the contribution of *GSY1* in mediating the rescue effect since it is significantly downregulated in the survived population **(Supplementary Figure 9f; upper right panel)** and also in our single knock-out screening assays, *gsy1Δ* cells exhibited positive growth even in the presence of α-factor **(Figure 3c-d)**. Last, we also evaluated the impact of LST alone (without α-factor treatment) on yeast cells via transcriptomics and observed significant differential expression of genes associated with vital cellular processing, validating the bioactivity of LST **(Figure 5f; middle panel, Supplementary Figure 9f; middle panel)**. Last, to dissect the role of LST in mediating resistive response toward α-factor treatment, we analyzed transcriptomes of yeast cells (pre-loaded or unloaded with LST) with and without α-factor treatment and did not observe any prominent mating or apoptosis-related genes among the differentially expressed genes. These results further highlight that the innate resistive response toward the alpha factor operates at the structural level rather than at the gene expression level **(Figure 5f; right panel, Supplementary Figure 9f; lower panel)**. This is also in line with our computational analysis, as discussed above.

Since our intensive computational interrogation of all the available human GPCR-Gα complexes revealed a higher degree of functional conservation **(Figure 1i, j)**, we next asked whether the identified allosteric, intracellular metabolic modulators such as ubiquinone 6 (CoQ6), zymosterol (ZST), lanosterol (LST), fucosterol (FST), and ubiquinone 10 (CoQ10) could also modulate human GPCR signaling since we observed a higher degree of conservation at the sequence, structural and functional level across the available GPCR-Gα interfaces of available complexes from the PDB Bank **(Figure 1 e-j)**. In other words, we intended to investigate whether sterols *per se* could intrinsically and intracellularly modulate the GPCR activity in higher vertebrates as well. To test this hypothesis, we first performed the computational analysis on the human and rat beta1/2-adrenergic receptors. Briefly, by using Gcoupler, we identified the putative GPCR-Gα interface and performed molecular docking with the aforementioned metabolites **(Supplementary Figure 10b-c)**. Docking results revealed a high binding affinity of these selected metabolites at the GPCR-Gα interface of adrenergic receptors, reminiscent of Ste2p-metabolite interactions **(Supplementary Figure 10b-c)**. To further evaluate the evolutionary conservation, we performed a sequence conservation analysis (computational) with the Ste2p (yeast) and adrenergic receptors from humans and rats. Careful inspection of the GPCR-Gα interface, particularly the metabolites-GPCR interaction contributing residues, revealed a high degree of conservation **(Supplementary Figure 10a)**. Finally, to elucidate the functional relevance

of this predicted interaction, we selected isoproterenol-induced, adrenergic receptor-mediated cardiac hypertrophy models in cultured human cardiac cell line (AC16) and primary neonatal rat cardiomyocytes **(Figure 5h)**. Our results suggest that both the human AC16 cell line and primary neonatal cardiomyocytes preloaded with these metabolites attenuate the isoproterenol-induced hypertrophic response as inferred from the quantitative analysis of the single cardiomyocytes' surface area **(Figure 5h-j)**. Taken together, these results collectively reinforce that modulation of GPCR activity by endogenous intracellular metabolites is an evolutionarily conserved phenomenon.

DISCUSSION

Over the last few decades, a tremendous amount of research has been conducted to identify the allosteric modulators of GPCRs [7,20]. Due to their relevance in drug discovery, most of the examples belong to the exogenous allosteric modulators [3,4,6–8,20]. The intracellular side of the GPCRs is exposed to the cytosol and, therefore allows binding to the signaling proteins such as trimeric G-proteins and arrestins [1,5,8]. In addition to these ubiquitous binders, the GPCR-Gα interface or other adjoining intracellular sites can also be targeted by chemically heterogeneous modulators, for example, GPCR-directed autoantibodies, Pepducins, sodium ions, etc.; however, the underlying mechanism of their mode of action is still elusive [4–6,8,9,11–13,65]. Systematic interrogation of allosteric sites, including the GPCR-Gα interface or nearby regions, demands multiple resource-intensive computational tools, in-depth technical skills, and domain knowledge [14,19,40]. While methods such as conventional computational structural biology or empirical machine learning approaches can be used to identify novel intracellular allosteric modulators of GPCRs, unfortunately, due to the lack of information about compounds regulating novel allosteric sites, implementation of these approaches is mainly unfeasible [66–69]. Here, we developed Gcoupler, a computational framework that harnesses the power of *de novo* cavity identification on GPCR topological surface and subsequent *in-silico* ligand synthesis, coupled with rigorous statistical methods for segregating synthesized compounds into high-affinity and low-affinity binders. Finally, the deep learning (Graph Neural Networks) algorithms in Gcoupler empower predictive modeling and allow large-scale screening of the user-queried compounds. Interestingly, unlike other ML/DL-based approaches, Gcoupler also offers a novel approach that not only alleviates the need for cavity-specific experimentally validated compounds for model training but also offers an efficient way for the large-scale screening of the user-specified compounds in a hassle-free manner. Moreover, due to its generic design, Gcoupler, in principle, can be used for non-GPCR proteins as well.

We used Gcoupler to discover the molecular basis of innate resistance towards α-factor-induced programmed cell death (PCD) in yeast [31,33,34,60]. Unlike the human genome that encodes ~800 GPCRs, the yeast genome possesses only two GPCR systems that allow pheromone and glucose sensing [70]. The pheromone-sensing pathway in yeast has been significantly interrogated over the last few decades, leading to the identification of feedback inhibition systems involved in this pathway; however, to the best of our knowledge, the majority of the known regulatory mechanisms operate downstream of the signaling cascade [29,34]. This further suggests that the rescue mechanism that imparts innate resistance towards α-factor-induced PCD might operate much upstream of the signaling cascade via a direct, physical interaction-based regulatory mechanism, in contrast to transcriptome/epigenome-mediated feedback mechanisms that might be comparatively slower. One such case could be the regulation at the receptor level via the endogenous metabolites that can intracellularly induce allosteric modulation of the Ste2 protein. This could be feasible since a handful of biochemically diverse, endogenous intracellular allosteric modulators for different GPCRs are reported in the literature [8–10]. Gcoupler enabled pinpointing a subset of cellular metabolites that could physically bind to the Ste2p-miniGpa1 interface and regulate the downstream signaling pathway [54]. Experimental evidence further strengthens the link between these selective metabolites and Ste2p-mediated signaling.

While the present evidence from this work demonstrates this interlink; however, it possesses certain limitations. First, while genetic screening for single metabolic mutants hints towards this interlink, it is still unknown whether the observed deviations in the α-factor mediated PCD are metabolite-mediated or have emerged from the pleiotropic effect in these mutants. Second, the concentrations of the metabolites used in the exogenous treatment experiments might not be the same as those present in natural conditions. Third, the interaction between metabolites (ZST, CoQ6, and LST) and Ste2p was only observed *in-silico* and demands further experimental proof involving FRET or BRET-based assays [16]. Fourth, the metabolites-protein interaction predictions can be substantiated by the mutagenesis experiments of the IC4 and IC5 residues; however, such experiments might further complicate the interpretation and pose challenges to elucidate whether the speculative mutation-based activity loss is due to interference with trimeric G-protein binding or metabolites-induced binding enhancement or hindrance. Of note, previous mutagenesis experiments revealed multiple critical amino acid residues that overlap with IC4 and IC5, suggesting their functional relevance in Ste2p downstream signaling **(Supplementary Table 7).** Fifth, the RNA-sequencing results revealed some of the potential genes that could assist the observed innate resistance response towards the α-factor; however, a series of

biochemical assays are required to be conducted on both the loss (knock-out/down) and gain (over-expression) of function mutants for these genes for further confirmation. Finally, it is technically challenging to assess the specificity of the observed mechanism by using another yeast GPCR system (Gpr1p) due to the high level of sequence, structural, and functional conservation of the GPCR-Gα interface.

Functional characterization of sterol biosynthesis intermediate (*ergΔ*) mutants revealed impaired mating response. Mechanistic insights further revealed that the underlying phenotypic defects are highly heterogeneous and range from defective schmoo morphology, reduced sterol accumulation at the mating projection tip, impaired membrane fusion, and lower expression levels of *FUS1* [71–75]. The present study uncovers a new molecular mechanism that provides a novel function of cellular sterols and also explains the underlying reason for the reduced efficiency of mating-dependent yeast microbial cell factories or biosensors in mutants with altered sterol levels [76,77]. Notably, in addition to the Ste2p regulation by endogenous intracellular sterols, their dysregulation also imparts tolerance to mycotoxic compounds, ethanol, and high temperatures; however, the underlying mechanism is largely elusive [78].

Since sterols facilitate many distinct biological functions, their *in vivo* functional characterization, such as co-measurement of their interactions with cellular proteins and induced phenotypic changes, is technically challenging. The present study utilizes both computational and experimental approaches and shows that sterols, alongside other endogenous metabolites, can target the conserved Gα binding sites of GPCRs and modulate their activity. The human and rat cell-based hypertrophy experiments further reinforce the specificity of this evolutionary conserved regulatory mechanism. In summary, in addition to uncovering a novel GPCR regulatory mechanism by endogenous intracellular metabolites, the present study proposes a novel computational approach that could accelerate and maximize our understanding of multiple unexplored allosteric sites of GPCRs. Based on the observed results from the computational and experimental analysis, the most plausible working model is that GPCRs can be intrinsically regulated via their Gα-binding interface via intracellular metabolites. The pre-binding of the selective metabolites to the intracellular GPCR-Gα interface might induce a local conformational change at the interface, facilitating the formation of a stable GPCR-G-protein complex and hence may obstruct the downstream signaling. However, one could not rule out the other possibilities, such as the influence on the orthosteric site by the metabolite binding at the GPCR-Gα interface, direct modulation of kinase or arrestin binding via the metabolites, and via

alternations in plasma membrane composition/dynamics by these hydrophobic metabolites. All these demand further rigorous interrogations.

MATERIAL AND METHODS

Backend code for the Gcoupler

The back-end code for the Gcoupler is written entirely in Python (3.8). The Gcoupler workflow consists of three distinct modules, namely, Synthesizer, Authenticator, and Generator. The Synthesizer module leverages the LigBuilder V3.0 [41] to identify the putative cavities on the protein surface with the potential to be an active or an allosteric site and perform *de novo in-silico* drug synthesis within the target cavity by following a hybrid approach of GROW and LINK method using Genetic Algorithm. Notably, among all the predicted cavities, the Synthesizer module pinpoints one cavity as the target for the subsequent *in-silico* ligand synthesis process. The decision is autonomous in nature and is taken based on user-supplied residue-position pairs of interest. The Synthesizer module employs the CAVITY (a structure-based protein binding site detection program) function of LigBuilder V3 for cavity detection [27]. It creates 3D grid points at a cushion of 0.5 Å to contain the whole protein and uses a Tripos force field [79] to categorize these points into three groups: 'occupied grid points,' which contain protein atoms or lie within the range of solvent-accessible radii; 'vacant grid points,' located outside the protein atoms; and 'surface grid points,' positioned between the occupied and vacant grid points. Following this classification, a geometric approach is employed to identify potential sites accessible to ligands, also influenced by factors such as depth and volume. Finally, both geometric structural information and physical chemistry properties are utilized to pinpoint locations for ligand binding sites and to quantitatively assess the feasibility of drug binding within each potential site. Gcoupler identifies multiple potentially orthosteric and allosteric cavities across GPCR topological surfaces and allows users to select one of them (per run). Users are provided with three options to choose cavities in the Gcoupler: (1) one of the identified cavities from the Gcoupler, (2) providing key amino acids to receive cavity suggestions, or utilizing third-party tools for cavity identification and providing amino acid information. Synthesizer also performs *in-silico de novo* synthesis of the active compounds within the target cavity, complementing the pharmacophores in the cartesian space based on the target cavity. In summary, Synthesizer, the first module, generates and outputs the simplified molecular-input

line-entry system (SMILES) and PDBQT files of the synthesized ligands along with cavity information in the form of grid coordinates, which is required as input by the next module.

Authenticator, the next module of Gcoupler, takes the PDBQT files and the cavity grid information generated using Synthesizer as input and further allows the segregation of these synthetic compounds based on their actual interaction at the molecular level. The Authenticator module leverages AutoDock Vina (1.2.3) python library for virtual screening [80]. The binding energies produced by the Authenticator module are further used to segregate the synthetic compounds into High-Affinity Binders (HABs) and Low-Affinity Binders (LABs) based on the distribution while preserving the class balance for the downstream deep learning steps. Of note, the default value of binding energy for the distribution split is set to -7 kcal/mol; however, the module provides enough flexibility to the users to try and test different cutoffs (loose to stringent) and can visualize the change in distribution and statistically compare the resulting distributions within the Gcoupler workflow.

The Authenticator uses the Kolmogorov-Smirnov test [42], Anderson-Darling test [44], and Epps-Singleton test [43] for hypothesis testing for the comparison of the distributions.

(1) Two Sample Kolmogorov-Smirnov test:

$$D_{m,n} = max_x |F(x) - G(x)|,$$

where,

$F(x)$ = observed cumulative distribution function of the first sample of size m

$G(x)$ = observed cumulative distribution function of the second sample of size n

(2) Anderson-Darling test:

$$ADK = \frac{n-1}{n^2(k-1)} \sum_{i=1}^{k} \left[\frac{1}{n_i} \sum_{j=1}^{L} h_j \frac{(nF_{ij} - n_i H_j)^2}{H_j(n - H_j) - \frac{nh_j}{4}} \right],$$

where,

h_j = the number of values in the combined samples equal to Z_j

H_j = the number of values in the combined samples less than Z_j plus one half the number of values in the combined samples equal to Z_j

F_{ij} = the number of values in the i-th group which are less than Z_j plus one half the number of values in this group which are equal to Z_j

k = the number of samples (groups)

n_i = the number of observations in group i

x_{ij} = the jth observation in the ith group, and

Z_j = Z_1, Z_2 ..., Z_L are the distinct values in the combined data set ordered from smallest to largest (L is less than n if there are tied observations)

(3) Epps-Singleton test:

Epps-Singleton test was used to compare the binding energies distributions of HAB and LAB. It returns a p-value that signifies the probability of falsely rejecting the null hypothesis (H_o) that both HAB and LAB are taken from the same population.

The Authenticator module supports the graphical plots, such as overlapping density plots and Empirical Cumulative Distribution Function (ECDF), to visualize the distributions. In case either the Authenticator module fails to recognize the default cutoff as an optimal threshold for the distribution split or the user decides that the resulting distributions fail to obtain the statistical inference under any threshold of their choice, the module is also incorporated with the other options for providing negative datasets, such as decoys (Gcoupler inbuilt function using Chem module of RDKit Python package [81]), and user-supplied negative datasets.

The last module of Gcoupler, known as Generator, leverages the DeepChem (2.6.1) [46] python library to build the Graph-Neural Networks supported classification models. The Generator takes the segregated HAB and LAB/decoys from the Authenticator module and uses these synthetic compounds to build prediction models. By default, the Generator module supports four different graph-based models, i.e., Graph Convolution Model (GCM), Graph Convolution Network (GCN) [82], Attentive FP (AFP) [83], and Graph Attention Network (GAT) [84], to generate classification models. Before the model-building step, the Generator module evaluates the class imbalance in the synthetic dataset and implements the upsampling techniques to counter it, if required. The Generator, by default, tests the pre-processed synthetic data on all four deep learning-based models under the default hyperparameters and returns models' performance parameter list, allowing users to select the best-performing model for the downstream refinement process. Users can either manually set up the hyperparameter tuning grid parameters or opt for the recommended grid range along with the fold count for k-fold cross-validation to tune the selected model around the best hyperparameters and evaluate the stability of the said optimized parameters. In the final step, the Generator builds the resultant model with the best-performing hyperparameters by utilizing the complete synthetic compound library (HAB + LAB/decoys)

for training, allowing large-scale screening of the user query compounds by using SMILES information.

In the post-data analysis framework, Gcoupler also supports a unique function for estimating the optimal probability threshold to narrow down the high-confidence hit compounds further. Gcoupler supports G-means and Youden's J statistics algorithms. The geometric mean (G-mean) is the mathematical square root of the product of sensitivity and specificity, whereas Youden's J Statistic (sensitivity+specificity−1) is defined as the distance between the ROC curve and the chance line. The optimal threshold is that which maximizes the J Statistics.

Runtime Analysis

To showcase the speed and efficiency of our *de novo* coupled Deep Learning approach against conventional docking, we performed a comparative study involving analysis of the same query compound dataset against a single target of interest through both approaches. A system with 125 GB RAM, 16 Threads, and 8 CPU cores with no upgradation to the software or hardware within the duration of this analysis was used as the platform for this comparison. To compare the time complexity between Gcoupler and classical docking procedures using AutoDock [48], we selected human alpha-1A adrenergic receptors (ADRA1A) as our GPCR of interest. Since the experimentally elucidated structure of ADRA1A is unknown, we used AlphaFold [85] predicted structure as our starting point. The ligand binding cavity at the extracellular site was determined using the LigBuilder V3.0 [41] cavity function. Moreover, we obtained the ADRA1A ligand information from the ChEMBL database (Version 31) corresponding to the accession ID: CHEMBL229 [49]. We obtained a total of 3684 bioactive compounds against ADRA1A; however, to ensure uniformity, we only selected those ligands (#933) that were annotated as "single protein format experiments". Files preparation for AutoDock-based docking includes conversion of ligand SMILES to MOL2 using OpenBabel (2.4.1) [86], followed by conversion of MOL2 to PDBQT via MGLtools (1.5.6) [87], and receptor PDB to PDBQT using OpenBabel (2.4.1) [86]. Noteworthily, the grid parameter calculations were manually performed, and docking was performed using AutoDock (4.2.6).

The Gcoupler workflow was performed as per the steps above. To ensure uniformity of the target cavity between both approaches, the cavity information along with the grid coordinate obtained during the initial steps of the AutoDock approach [48] was reused by the Synthesizer

and the Authenticator module for generating *de novo* ligands and their molecular interaction-based classification, respectively. The Authenticator module selected an optimal binding energy cutoff of -8 kcal/mol; however, we opted for decoys for the negative dataset generation due to severe class imbalance. Under default hyperparameters, AttentiveFP showed better overall performance scores among the four deep learning-based models tested. We used the AttentiveFP model with the following hyperparameters: {'num_layers': 2, 'num_timesteps': 2, 'graph_feat_size': 200, 'dropout': 0} after assessment with 10-fold cross-validation. The final model was generated using the complete HAB compound library as the positive and the respective decoys dataset as a negative class for the model learning. Post-model generation, all 933 ligands were screened for their binding prediction probabilities.

Gcoupler Benchmarking

Batch effect in the different runs of Gcoupler for a particular cavity was performed using the standard Gcoupler Docker image. Of note, intracellular cavity 4 (IC4) of the Ste2 protein of yeast was used for benchmarking. A total of 100 molecules were *in-silico* synthesized by the Synthesizer module of Gcoupler iteratively. Post-generation, atom pair fingerprints (ChemmineR; R package) were calculated for the synthesized molecules from each run, and the data was visualized using Principal Component Analysis (R package), and pairwise comparison using Tanimoto Similarity (ChemmineR, R package). Benchmarking of Gcoupler-generated models in classifying experimentally validated was performed using GPCRs taken from the DUD-E dataset, alongside the information about the active ligands and their randomly selected number-matched decoys [45]. Benchmarking of Gcoupler in identifying experimentally elucidated allosteric sites and their modulates was performed on the PDB complexes taken from RCSB PDB.

Sequence-Structural-Functional level analysis

All the available, non-redundant sixty-six human GPCR-Gα complexes were downloaded from the RCSB PDB database (https://www.rcsb.org/). The sequence level information for each of these GPCRs was obtained from the UniProt database (https://www.uniprot.org). Multiple Sequence Alignment was performed to study the sequence level conservation, using the FASTA sequences of the GPCRs as input for the MUltiple Sequence Comparison by Log-Expectation (MUSCLE) algorithm [88]. Of note, MUSCLE uses the PAM substitution matrix and sum-of-pairs (SP) score for alignment scoring. The MUSCLE alignment output in CLW format was then subsequently used to compute amino acid level conservation using the WebLogo tool (https://weblogo.berkeley.edu/logo.cgi). To identify conserved motifs native to the GPCR-Gα interface, residues at the GPCR-Gα interface for each GPCR-Gα

complex were retrieved using EMBL-EBI developed PDBePISA tool and subsequently mapped on the WebLogos [89]. To test the structural level conservation, the pairwise similarity of the PDBePISA provided GPCR-Gα interfaces (cavity) of all 66 GPCRs was achieved using the normalized Root Mean Square Deviation (RMSD), calculated using the PyMOL software (https://pymol.org/2/). The RMSD values were normalized by dividing the cavity RMSD with their respective whole protein RMSD. Finally, to analyze the functional level conservation of the GPCR-Gα interfaces, we used the Gcoupler's Synthesizer module to compute 50 synthetic ligands for each GPCR-Gα interface (cavity) and calculated their physicochemical properties (descriptors) using Mordred [90]. For each GPCR-Gα-protein interface, we computed a single vector representing the aggregated physicochemical property of all the synthesized compounds for the given GPCR cavity and measured their similarities using the Cosine similarity. Cosine similarity is a similarity measure between two non-zero vectors defined in an inner product space.

$$cosine\ similarity = \frac{\sum_{i=1}^{n} A_i B_i}{\sqrt{\sum_{i=1}^{n} A_i^2}\sqrt{\sum_{i=1}^{n} B_i^2}},$$

where, A_i and B_i are components of vectors A and B of size n respectively.

Molecular Dynamics Simulation

The Molecular Dynamics simulation was performed using either GROMACS [91] or AMBER [92] software suite. For Ste2p, the experimentally elucidated structure with PDB ID: 7ad3 was downloaded from the RCSB PDB database [54]. Since the available structure was provided for the dimer, PDB preprocessing steps were used to isolate a single chain (chain B) that refers to the GPCR. Embedding in the lipid bilayer representing yeast plasma membrane composition was performed using the CHARM-GUI [93], followed by the simulations using GROMACS [91]. Notably, we performed six rounds of equilibration with the membrane system and nine rounds of production runs of 5 ns each. We finally selected the last frame of the simulation step from the production run for further analysis. Protein-ligand complexes were prepared for the molecular dynamics simulations using AMBER software [92], as discussed above. Notably, we performed all analyses using the Ste2p monomers. The grid box center and several grids were chosen appropriately to restrict the conformational sampling within the specific binding site. By default, the software estimates docking energies for 2,50,000 conformations of the ligands within the binding sites and ranks them to find the top 10 binding modes. The best binding modes for the ligands in these two sites were analyzed. The subsequent molecular dynamics simulations were performed for the ligands in these two binding sites, and the input configuration is based on the aforementioned molecular docking study results. The charges for the ligands were computed using density functional theory calculations at the B3LYP/6-31+G* level of theory. We used a general amber force field

(GAFF) to describe the molecular interactions [94]. For protein, we employed FF19SB force-field [95], and for water, TIP3P force-field was used [96]. The Ste2p-ligand complexes were embedded in about 23,000 water molecules. The minimization run, simulation in the constant volume ensemble, and simulation in the isothermal-isobaric ensemble were carried out. The time step for integrating the equation of motion was 2 fs. Following the equilibration run, a time scale simulation for 100 ns (three replicates for IC4 and IC5) and 550 ns (one replicate for IC4 cavity only) was carried out. All the Ste2p-ligand complex simulations were performed using Amber20 software [92]. Various structural properties, such as RMSD and RMSF were computed and analyzed. The binding free energies using molecular mechanics-Generalizer Born surface area approach (MM/GBSA) were computed for 1000 configurations picked up from the last 10 ns trajectory. The binding free energies computed using the molecular mechanics-generalized Born surface area approach are the quantitative measure of the binding preference of ligands to a specific target binding site. The values are obtained from the time average of different contributions such as van der Waals, electrostatic, polar, and non-polar solvation energies. When compared to molecular docking approaches, these binding free energies are obtained as an average over multiple protein-ligand configurations from MD simulations and so are more reliable and accurate. In addition, many of the molecular docking simulations do not account for the conformational flexibility, but in the MM/GBSA calculations, the effects of protein-conformational flexibility, segmental motion, and cavity breathing are also accounted for, making results more reliable compared to molecular docking based binding affinities.

Molecular Docking (AutoDock)

YMDB metabolites were downloaded from the YMDB database (Version 2.0) [53]. Of note, we took the metabolites structure file (SDF format) provided on the YMDB database to extract 2D information of the metabolites, and to gain missing metadata, we intersected these metabolites with the YMDB full database and obtained a total of 1264 metabolites. When we finally converted these compounds into 3D structures for docking or into graphs for testing data for the DeepChem-based model, a fraction of these compounds failed to convert and we finally selected a unique set of 1198 metabolites. The file preparation for the docking protocol involved converting the YMDB SMILES (1D) to MOL2 (3D) format. This was achieved using the OpenBabel software (2.4.1) [86]. Further, the compounds from the MOL2 format were converted into dockable PDBQT format by following the MGLtools (1.5.6) ligand preparation procedure [87]. Of note, the sub-processing steps include detecting the ligand center, selecting single bonds as torsion/rotatable bonds, etc. As discussed above, the receptor PDBs were also converted into PDBQT format using the OpenBabel software [86].

AutoDock (4.2.6) [48] was used for molecular docking by implementing a Genetic algorithm with the following parameters (population size = 150, maximum number of evaluations = 2,50,00,000, and maximum number of generations = 27,000). Notably, ten complexes were generated per YMDB compound. The docking results, i.e., extracting the lowest binding energy from each docked protein-ligand complex, were analyzed using the MGLtools (1.5.6) [87]. Notably, the ΔG values were calculated on the pre-simulated stable docked structure. In the case of blind docking, the grid was made across the complete Ste2p structure and was docked using the aforementioned parameters with the YMDB metabolites.

Functional Enrichment Analysis

Functional enrichment analysis of the differentially enriched metabolites or the metabolites of interest was performed using MetaboAnalyst (https://www.metaboanalyst.ca/) web server [56]. In the case of the YMDB compound library, the union list of the lead compounds for each target cavity (IC4 & IC5) was used as input. In the case of the untargeted metabolomics data, the list of differentially enriched metabolites between the α-factor treated and untreated conditions was used as input. The hypergeometric test was used for hypothesis testing and providing subsequent p-values for each resultant enrichment pathway.

Protein-Protein Docking

To determine the impact of metabolite binding on GPCR-Gα and GPCR-α-factor interaction, we performed Protein-Protein docking using the HADDOCK (High Ambiguity Driven protein-protein DOCKing) webserver [97]. HADDOCK is an innovative information-guided, flexible docking methodology for biomolecular complex modeling, uniquely utilizing ambiguous interaction restraints (AIRs) derived from identified or predicted protein interfaces, along with explicit distance restraints (e.g., MS cross-links) and diverse experimental data like NMR residual dipolar couplings, pseudo contact shifts, and cryo-EM maps, setting it apart from ab-initio docking approaches. In the case of Ste2p-miniGpa1p or Ste2p–α-factor docking, the PDB chains of both proteins were extracted from the PDB complex (accession id: 7ad3) [54]. Ste2p in the docked complex with the respective metabolites were simulated via the AMBER software suite [92]. Post simulation, the most stable conformation of protein-metabolite was taken, and the metabolite was manually removed to obtain a metabolite-influenced stable Ste2p structure. HADDOCK was subsequently used for the protein-protein docking between wild Ste2p or metabolite-influenced bound stable Ste2p against miniGpa1-protein or α-factor (extracted from PDB ID: 7ad3). The optimal representative complexes were obtained from the HADDOCK results [97] and were used as input in PRODIGY (PROtein binDIng enerGY prediction) [98] for K_d and ΔG calculations. PRODIGY is a web service that provides support

for the prediction of binding affinity in biological complexes. Notably, the ΔG values were calculated on the pre-simulated stable docked structures.

Yeast strains

BY4741 *(MATa his3Δ1 leu2Δ0 met15Δ0 ura3Δ0*) and *ste2Δ* (*MATa ste2Δ::kanMX his3Δ1 leu2Δ0 ura3Δ0 met15Δ0*) strains of *Saccharomyces cerevisiae* were used in all the experiments. For the mating assay, BY4742 strain *(MAT*α *his3Δ1 leu2Δ0 lys2Δ0 ura3Δ0*) was also used. All the knockouts were obtained from the Yeast Deletion Collection (*MATa xxx::kanMX his3Δ1 leu2Δ0 ura3Δ0 met15Δ0*). Unless mentioned, the yeast was grown at 30 °C at 200 rpm in yeast extract–peptone–dextrose (YPD) (1% yeast extract, 2% peptone, and 2% dextrose). Agar (1.5%) was additionally added to YPD to prepare plates.

Metabolomics

Wildtype (BY4741) and *ste2Δ* yeast strains were inoculated in the primary culture, followed by a secondary culture, in YPD medium at 30 °C at 150 rpm for 16 hours each. 1.5 mL of the secondary cultures were aliquoted into a 96-well deep well plate to ensure an equal number of cells for both strains. α-factor (T6901, Sigma-Aldrich) was added to the wells to attain final concentrations of 10 μM, 20 μM, 30 μM, 40 μM and 50 μM, with eight biological replicates each. DMSO (28580, SRL) (volume equivalent to the 30 μM α-factor sample) was added to the solvent control. DMSO or α-factor was not added to untreated (WT) and *ste2Δ* conditions. The plate was covered with a breathe-easy membrane (Z380059, Sigma-Aldrich) and incubated at 30 °C at 150 rpm for 4 hours. After incubation, an aliquot of 50 μL was used to perform Propidium Iodide (PI) fluorometric assay as described in the later section.

Post Propidium Iodide-based cell viability assay, four biological replicates were created by pooling biological replicates. These were transferred to 1.5 mL microcentrifuge tubes and pelleted down at 6000 rpm for 5 minutes at room temperature (RT). The cell pellet was treated with zymolyase enzyme (L2524, Sigma-Aldrich) at a final concentration of 40 units/mL in 1X PBS and incubated at 30 °C for 1 hour. Following this, the cells were washed with 1X PBS, and the cell pellet was stored at -80 °C before metabolomics.

Metabolomics was performed on 1290 Infinity HPLC coupled with 6545 QTOF (Agilent Technologies, Santa Clara, CA, USA) equipped with dual ESI Source. The internal controls used in metabolomics include Jasmonic acid, Gibberellic acid, zeatin, Tryptophan 15N, Estrone D4, Arginine 15N, Thiamine D4, 15N5-8-OH-2-dG, 13C12 dityrosine, and 8-PGF2-D4. For the sample preparation, the protein precipitation method was used. Briefly, 10 μL of

a cocktail containing commercial stable isotopes internal standards were added, followed by the addition of chilled 750 µL methanol: water (4:1) and probe sonicated. Then, 450 µL of chilled chloroform was added and vortexed for 5 min, followed by adding 150 µL of chilled water, vortexed, and kept the sample at -20 ^{o}C for 30 min. Next, samples were centrifuged at 5000 rpm at 4 °C for 10 min to separate the methanol and chloroform layers. Both layers were collected and dried at 30 °C using a vacuum concentrator and reconstituted in 100 µL methanol: water (1:1). Quality Control (QC) samples were injected between every five samples to check the drift in the instrument and to evaluate the signal repeatability. Pearson's rank order showed that QCs (n = 6) were strongly correlated(r>0.9) with each other, suggesting variations were insignificant.

Data analysis of the metabolomics data includes peak normalization. Furthermore, the normalized peak intensities of all the samples' replicates were merged, and the metabolites with a constant value or with more than 50% missing values were omitted. The missing values were imputed using the feature-based k nearest neighbors (kNN) via Metaboanalyst webserver. The data were filtered based on the interquartile range (IQR). To find the list of Differentially Enriched Metabolites (DEMs), $\log_2$ fold change ($\log_2$FC) values were calculated for each sample with respect to the solvent control, along with its statistical significance student's t-test. The metabolites with $|\log_2 FC \geq 1|$ and p-value < 0.05 were considered DEMs. Pathway Over Representation Analysis (ORA) was performed using MetaboAnalyst [56]. Note ORA is a computational method used in metabolomics research to gain insights into the biological significance of a set of metabolites that exhibit changes under different experimental conditions or in response to a perturbation or those belonging to a particular group. This analysis is conducted using statistical tests such as hypergeometric tests or Fisher's exact tests to determine if the observed number of metabolites in a given pathway is significantly higher than what would be expected based on the background distribution of metabolites.

Genetic Screening

Fifty-three knockout strains from the Yeast Deletion Collection, along with WT and *ste2Δ* strains, were grown in primary culture, followed by secondary culture, in YPD medium at 30 °C at 150 rpm for 16 hours each. Ensuring an equal number of cells in all the strains, 5 µL of secondary culture was inoculated into 96-well plates containing 145 µL of YPD and grown for 16 hours at 30 °C at 200 rpm with eight biological replicates. Afterward, the α-factor was added to half the replicates at a final concentration of 30 µM. An equal volume of DMSO was

added to the other half to serve as solvent control. The plates were incubated for another 4 hours. After incubation, a 50 µL aliquot was mixed with 50 µL of staining solution (Propidium Iodide (PI; 11195, SRL) in 1x PBS, freshly prepared) to attain a final PI concentration of 5 µg/mL in 96-well black plates. The plates were incubated in the dark for 15 minutes. Heat-killed (HK) cells were used as a positive control. The fluorescence was measured using Biotek Synergy HTX multi-mode reader at excitation and emission wavelengths of 530/25 nm and 590/25 nm, respectively. Another 50 µL aliquot from the original plates was used to measure OD_{600} after 1:2 dilution with 1X PBS. The fluorescence values were first normalized for data analysis with the blank normalized OD_{600} values of the respective well. These normalized fluorescence values were subjected to two more rounds of normalization, first with unstained cells followed by heat-killed cells. Following this, percentage fold change was calculated for the treated group with respect to the untreated group. The p-value was computed using a one-sample student's t-test.

Cell viability Assay using Growth Kinetics

Wildtype and *ste2Δ* yeast strains were grown in primary culture, followed by secondary culture, in YPD medium at 30 °C at 200 rpm for 16 hours each. Ensuring an equal number of cells for both strains, 5 µL of secondary culture was inoculated into a 96-well plate containing 145 µL of YPD along with respective metabolites (CoQ6: Coenzyme Q6, 900150O, Avanti® Polar Lipids, Sigma-Aldrich; ZST: Zymosterol, 700068P, Avanti® Polar Lipids, Sigma-Aldrich; and LST: Lanosterol, L5768, Sigma-Aldrich) at concentrations of 0.1 µM, 1 µM, and 10 µM each and grown for 24 hours at 30 °C at 200 rpm with multiple biological replicates. An equal volume of ethanol was added to the control group to negate the effects of the solvent. After incubation, 5 µL cultures from this plate were used as an inoculum for another 96-well plate containing 145 µL of YPD along with respective metabolites (CoQ6, ZST, and LST) at concentrations of 0.1 µM, 1 µM, and 10 µM each in the presence of 10 µM α-factor (T6901, Sigma-Aldrich) in the treated group and DMSO (28580, SRL) in the untreated group with multiple biological replicates. The plates were sealed with breathe-easy membranes to prevent evaporation. The growth kinetics was performed in a Biotek Synergy HTX multi-mode reader for 16.5 hours at 30 °C under continuous orbital shaking at 559 CPM. Absorbance was measured at 600 nm every 30 minutes. The area under the curve (AUC) was calculated for each sample using the bayestestR package in R with default parameters and normalized using the OD_{600} value at time t=0.

Cell viability Assay using Propidium Iodide

Wildtype and *ste2Δ* yeast strains were grown in primary culture, followed by secondary culture, in YPD medium at 30 °C at 200 rpm for 16 hours each. Ensuring an equal number of cells for both strains, 5 µL of secondary culture was inoculated into a 96-well plate containing 145 µL of YPD along with respective metabolites (CoQ6, ZST, and LST) at concentrations of 0.1 µM, 1 µM, and 10 µM each and grown for 24 hours at 30 °C at 200 rpm with multiple biological replicates. An equal volume of ethanol was added to the control group to negate the effects of the solvent. Following this, the α-factor was added to half the wells at a final concentration of 30 µM. An equal volume of DMSO was added to the other half to serve as solvent control. The plates were incubated for another 4 hours. After incubation, a 50 µL aliquot was mixed with 50 µL of staining solution (Propidium Iodide (PI) in 1X PBS, freshly prepared) to attain a final PI concentration of 5 µg/mL in 96 well-black plates. The plates were incubated in the dark for 15 minutes. Heat-killed (HK) cells were used as a positive control. The fluorescence was measured using Biotek Synergy HTX multi-mode reader at excitation and emission wavelengths of 530/25 nm and 590/25 nm, respectively. Another 50 µL aliquot from the original plate was used to measure OD_{600} after 1:2 dilution with 1X PBS.

The fluorescence values were first normalized for data analysis with the blank normalized OD_{600} values of the respective well. Cellular background fluorescence values of the unstained cells were subtracted from these normalized fluorescence values. Post this, fold change between the untreated solvent control and the α-factor treated samples was computed by dividing the latter with the former. Mann Whitney U-test was used to measure the statistical significance.

Cell viability Assay using FUN™1 staining

Wildtype and *ste2Δ* yeast strains were grown in primary culture, followed by secondary culture, in YPD medium at 30 °C at 150 rpm for 16 hours each. Ensuring an equal number of cells for both strains, 5 µL of secondary culture was inoculated into a 96-well plate containing 145 µL of YPD along with respective metabolites at concentrations of 1 µM (ZST and LST), and 10 µM (CoQ6) and grown for 24 hours at 30 °C at 150 rpm with nine biological replicates. An equal volume of ethanol was added to the control group to negate the effects of the solvent. Following this, α-factor (T6901, Sigma-Aldrich) was added to a third of the wells at a final concentration of 30 µM, acetic acid (85801, SRL) to another third at a final concentration of 199 mM, and DMSO to the remaining third to serve as solvent control. The plates were incubated for another 4 hours. Post incubation, the cells were

pelleted down and washed with 1X PBS to remove any media traces at 6000 rpm for 5 minutes at RT. The staining solution was freshly prepared in 1X GH solution (10 mM HEPES buffer, pH 7.2, 2% glucose) with FUN™ 1 Cell Stain (F7030, Invitrogen) at a final concentration of 5 µM. The samples were incubated in the dark for 30 minutes, centrifuged at 6000 rpm for 5 minutes, and the pellet resuspended in 25 µL of 1x GH solution. 5 µL of the sample was used for fluorescence microscopy (Nikon Eclipse Ci-L Fluorescence Microscope with Nikon DS-Qi2 camera). FITC and TRITC filters were used for measuring green and red fluorescence, respectively, with an exposure time of 1 second each. For each sample, the number of cells with red and green fluorescence, indicating cellular viability and vitality in each image, were counted using ImageJ and normalized with the total cell counts.

Mating Assay

BY4741 (*MATa*), BY4742 (*MATα*), and *ste2Δ* yeast strains were grown in primary culture, followed by secondary culture, in YPD medium at 30 °C at 200 rpm for 16 hours each. Ensuring an equal number of cells for both strains, 5 µL of secondary culture was inoculated into a 96-well plate containing 145 µL of YPD along with respective metabolites at concentrations of 1 µM (ZST and LST) and 10 µM (CoQ6) and grown for 24 hours at 30 °C at 200 rpm with 3 biological replicates. An equal volume of ethanol was added to the control group to negate the effects of the solvent. After 24 hours, the cells were harvested and washed with fresh YPD at 6000 rpm for 5 minutes at RT to remove all traces of metabolites. The pellet was resuspended in fresh YPD. After ensuring the number of cells is equal in all the samples, 100 µL of MATa cells were mixed with 100 µL of MATα in a 96-well plate, mixed thoroughly, covered with breathe-easy membrane, and incubated at 30 °C at 200 rpm for 4 hours for mating. After mating, the cells were harvested and washed with distilled water at 6000 rpm for 5 minutes at RT to remove all media traces. Following this, the cells were resuspended in 200 µL of distilled water, serial dilutions of 1:10 were prepared in distilled water, and 5 µL culture was spotted on the SC-Met (His, Leu, Ade, Ura, Lys), SC-Lys (His, Leu, Ade, Ura, Met), and SC-Met-Lys (His, Leu, Ade, Ura) agar plates each in 3 technical replicates. Composition of the SC agar plates: 2% glucose, 2% agar, 20 mg/L histidine, 120 mg/L leucine, 60 mg/L lysine, 20 mg/L methionine, 20 mg/L uracil, and 20 mg/L adenine. The plates were incubated at 30 °C for two days.

After incubation, the colonies were counted in ImageJ in the 10^4 dilutions, which had the best resolution of colonies. Mating efficiency was calculated using the following formula:

$$Mating\ Efficiency = \frac{colonies\ in\ DD\ \times\ Dilution\ Factor}{colonies\ in\ SD\ \times\ Dilution\ Factor} \times 100$$

where, SD is single dropout media (SC-Met for MATα, and SC-Lys for MATa), and DD is double dropout (SC-Met-Lys).

RNA-Sequencing

Yeast cells (BY4741) were grown at 30 °C at 200 rpm in YPD medium in biological duplicates in the presence or absence of lanosterol (LST) at a final concentration of 1 μM. Post-metabolite loading, the cells were either treated or untreated with the α-factor at a final concentration of 30 μM for 2 hours at desired growth conditions. Post these steps, the cells were harvested, and RNA was isolated using the protocol described in Mittal et al. [99].

Following sequencing, we conducted a quality control check with MultiFastQ. The paired-end sequencing reads were aligned to the yeast reference genome (ENSEMBL; R64-1-1; GCA_000146045.2) via the align function of the Rsubread package (v.2.6.4), generating aligned BAM files. Before mapping, read trimming was performed at both ends. An expression matrix was produced with the featureCounts function to contain raw read counts for each sample. The read count matrix was normalized using TMM (trimmed mean of M values) normalization (**Supplementary Table 8**), and the differential gene expression analysis was performed using NOISeq (v2.38.0) [100] (**Supplementary Tables 9-11**). The functional gene ontology analysis was performed using the Gene Ontology Term Finder tool (Version 0.86) of the Saccharomyces Genome Database (https://www.yeastgenome.org). The normalized read count matrix and the raw FASTQ files are available at the Zenodo repository.

Ethical statement

The local IAEC (Institutional Animal Ethics Committee) committee at CSIR-Central Drug Research Institute approved all the animal experiments (IAEC/2020/38) following the guidelines of the Committee for the Purpose of Control and Supervision of Experiments on Animals (CPCSEA), New Delhi, Government of India.

Cardiomyocytes Hypertrophy Models

Human cardiomyocyte cell line AC16 was cultured in DMEM-F12 (Thermo Scientific) with 12.5% fetal bovine serum (Thermo Scientific) at 37°C in the presence of 5% CO_2. AC16 cells were seeded in a 24-well cell culture plate for cell size measurements. After 24 hours, cells

were treated with metabolites (CoQ6, ZST, LST, FST (F5379, Sigma-Aldrich), CoQ10 (15039, SRL)) at the final concentration of 2.5 μM in the presence of 1% fetal bovine serum (FBS) and incubated overnight. The next day, the medium was changed. Fresh metabolites were added at 2.5 μM final concentration and isoproterenol treatment at 25 μM concentration and incubated for 48 hours in the presence of 1% FBS. Next, cells were washed with 1X PBS, fixed with 4% paraformaldehyde, and stained with wheat germ agglutinin (Thermo Scientific) and DAPI. Images were taken by Leica DMI 6000 B (Leica Microsystems, USA) at 20X objective. Cell area was calculated by using ImageJ software.

Neonatal rat cardiomyocytes were isolated from one to three-day-old SD rat pups using Collagenase Type II. Briefly, pups were sacrificed, hearts were explanted, washed in 1X PBS, and chopped into small pieces. Chopped heart pieces were digested with Collagenase Type II at 1 mg/mL (Thermo Scientific, USA) at 37°C. Digested cells are centrifuged, resuspended in a DMEM medium, and pre-plated for 90 minutes to remove fibroblasts. Cardiomyocytes containing supernatant were then collected and seeded in a gelatin-coated 24-well cell culture plate coated. After 48 hours later, cells were washed with 1X PBS and incubated with metabolites at a concentration of 2.5 μM overnight in the presence of 1% FBS. The next day, the medium was changed, and cells were treated with metabolites (2.5 μM) and isoproterenol (10 μM) in the presence of 1% FBS. After 72 hours, cells were fixed and stained with alpha-sarcomeric actinin (#MA1- 22863 Thermo Scientific, USA) and DAPI. Images were taken by Leica DMI 6000 B (Leica Microsystems, USA) at 20X objective. Cell area was calculated by using ImageJ software.

Statistical Analysis

All statistical analyses were performed using either the Past4 software [101] or R-Programming [102]. Mann-Whitney U test was used to compare the medians of the two distributions (non-parametric), while Student's t-test was used for comparing the means (pairwise comparisons). In the case of p-value correction, the Bonferroni method of p-value adjustment is used wherever required. The p-value cutoff used in this study is 0.05. *, **, ***, and **** refer to p-values <0.05, <0.01, <0.001, and <0.0001, respectively.

Data Availability

The processed untargeted metabolomics data is provided as Supplementary Information. The raw RNA sequencing files are available at ArrayExpress under accession *E-MTAB-12992*. The raw data files are available from the lead author upon request.

Code Availability

A Python package for Gcoupler is provided via pip https://test.pypi.org/project/Gcoupler/. A docker container pre-compiled with Gcoupler and all of its dependencies can be found at https://hub.docker.com/r/sanjayk741/gcoupler. The source code of Gcoupler is available on the project GitHub page: https://github.com/the-ahuja-lab/Gcoupler and also at Zenodo with DOI: 10.5281/zenodo.7835335, whereas the raw sequencing files can be assessed using DOI: 10.5281/zenodo.7834294.

Conflict of Interest

The authors declare that they have no competing interests.

Acknowledgments

The authors thank the IT-HelpDesk team of IIIT-Delhi for assisting with the computational resources. We thank all the members of the Ahuja lab for their intellectual contributions at various stages of this project. We thank Prof. G.P.S Raghava for providing critical comments on our manuscript. We thank Dr. Arjun Ray for providing intellectual support. We also thank Dr. Martin Graef and Dr. Kaushik Chakraborty for sharing yeast strains and the NIPER Guwahati central facility for helping us with high-resolution metabolomics. The Ahuja lab is supported by the Ramalingaswami Re-entry Fellowship (BT/HRD/35/02/2006), a re-entry scheme of the Department of Biotechnology, Ministry of Science & Technology, Government of India, Start-Up Research Grant (SRG/2020/000232) from the Science and Engineering Research Board, and a research grant from IHUB Anubhuti (Project Grant/23) and an intramural Start-up grant from Indraprastha Institute of Information Technology-Delhi. The INSPIRE faculty grant from the Department of Science & Technology, India, funds the Sengupta lab. Gupta Lab is funded by the Ramalingaswami Re-entry Fellowship (BT/RLF/re-entry/14/2019) from the Department of Biotechnology, Government of India.

Author Contributions

The study was conceived by G.A. Computational analysis workflows were designed by G.A. Statistical guidance was provided by D.S. Docking, and Molecular Simulations were supervised by N.A.M and conducted by N.A.M, and S.K.M. Data analysis was performed by S.K.M., A.M., S.S., S.K., S.D., S.A., V.G., T.S.G., N.K.D and K.S.. S.K.M built the Gcoupler Python package. G.A. and A.M. designed yeast experimental workflows and performed by A.M. Human cell culture-based experiments were performed and analyzed by A.G., and

S.K.G. Illustrations were drafted by A.M., S.K.M., and G.A. G.A. wrote the paper. All authors have read and approved the manuscript.

FIGURE LEGENDS

Figure 1: Development of the Gcoupler computational package to decode GPCR-Gα-protein interface topology.

(a) Schematic workflow depicting the main modules implemented in the Gcoupler package. Of note, Gcoupler possesses three major modules, i.e., Synthesizer, Authenticator, and Generator. Synthesizer takes the users' information about the GPCR of interest in the PDB format. It also takes the key residues which can be used for cavity annotation. Synthesizer allows generation of *de novo* design of the synthetic ligands based on the cavity topology. Authenticator, the second module, allows the screening of these synthetic ligands via a virtual screening approach. It also supports inferential statistics and graphical methods for statistics and data visualization, respectively. Generator, the last module, allows building the classification models for large-scale screening of the user-provided compounds. **(b)** Molecular representation depicting the indicated experimentally validated orthosteric sites of the indicated GPCRs, with the zoom-in inlet on the right highlighting the ligand and the cavity topologies. **(c)** Confusion matrices indicating the relative proportions of experimentally determined ligands and their respective decoys (randomly selected to match # of ligands for each receptor). Note the number of active ligands and decoys is mentioned at the bottom. **(d)** Schematic workflow depicting the major steps in determining the sequence, structural, and functional conservation of the human GPCRs-Gα-protein interfaces. **(e)** Snakeplot depicting the standard human GPCR two-dimensional sequence level information. Conserved motifs of the GPCR-Gα-protein interfaces are depicted as WebLogo. Asterisks represent residues of conserved motifs present in the GPCRs-Gα-protein interfaces. Of note, the location of the motifs indicated in the exemplary GPCR snake plot is approximated. **(f)** Schematic workflow illustrates the steps in measuring and comparing the structural conservation of the GPCR-Gα-protein interfaces across human GPCRs. **(g)** Representative structures of the proteins depicting highly conserved (low RMSD) and highly divergent (high RMSD) GPCR-Gα-protein interfaces. PDB accession numbers are indicated at the bottom. **(h)** Heatmap depicting the RMSD values obtained by comparing all the GPCR-Gα-protein interfaces of the available human GPCRs from the protein databank. Of note, the RMSD of the Gα-protein cavity was normalized with the RMSDs of the respective whole proteins across all pairwise comparisons. **(i)** Heatmap depicting the pairwise cosine similarities

between the *in-silico* synthesized ligands of the GPCR-Gα-protein interfaces of the available human GPCRs using Gcoupler.

Figure 2: Gcoupler predicted endogenous metabolic modulators of Ste2p.

(a) Schematic diagram depicting the hypothesis that the intracellular yeast metabolites could allosterically modulate the GPCR-Gα-protein (Ste2p-Gpa1p) interface and, therefore, the programmed cell death pathway in yeast. **(b)** Overlapping Ste2p (GPCR) ribbon diagram depicting the structural similarity between the experimentally elucidated Ste2p structure before and after molecular dynamics simulation using GROMCS software. RMSD value is depicted at the bottom. **(c)** Schematic diagram depicting the topology of all the cavities identified using the Synthesizer module of the Gcoupler python package. Of note, the cavity nomenclature includes the cavity location, i.e., EC (extracellular), IC (intracellular), and TM (transmembrane), succeeded by numerical number. **(d)** Diagram depicting the three-dimensional view of the Ste2 protein, with highlighted Gα-protein binding site (Gpa1) and the Gcoupler intracellular cavities (IC4 and IC5). The bar plot at the bottom depicts the percentage overlap at the amino acid levels between the Gα-binding site and predicted IC4 and IC5. **(e)** Schematic representation of the overall workflow used to predict the endogenous intracellular allosteric modulators of Ste2 receptor using Gcoupler and molecular docking technique. Of note, Yeast Metabolome DataBase (YMDB) metabolites were used as query compounds. **(f)** Overlapping density plots depicting and comparing the distributions of synthetic compounds predicted to target the IC4 and IC5 of the Ste2 receptor using the Gcoupler package. Of note, the Authenticator module of Gcoupler segregated the synthesized compound for each cavity (IC4 or IC5) into High-Affinity Binders (HAB) and Low-Affinity Binders (LAB). **(g)** AUC (Area under the curve) plots representing the performance of the indicated models. Notably, the models were trained using the cavity-specific synthetic compounds generated using the Gcoupler package. **(h)** Scatter plots depicting the relationship (correlation) between the binding prediction probabilities using Gcoupler and binding free energies computed using molecular docking (AutoDock). **(i)** Heatmap illustrating the relative enrichment of the indicated functional groups (RNH2: primary amine, R2NH: secondary amine, R3N: tertiary amine, ROPO3: monophosphate, ROH: alcohol, RCHO: aldehyde, RCOR: ketone, RCOOH: carboxylic acid, RCOOR: ester, ROR: ether, RCCH: terminal alkyne, RCN: nitrile) among the endogenous intracellular allosteric modulators (metabolites) of Ste2 receptor across IC4 and IC5. **(j)** Scatterplot depicting the Pathway Over Representation Analysis (ORA) results of the endogenous metabolites that were predicted to bind to the GPCR-Gα-protein (Ste2p-Gpa1p) interface

using both Gcoupler and molecular docking. Structures of the top enriched endogenous metabolites are depicted on the right.

Figure 3: Metabolomics and metabolic mutant screening unveil the link between metabolism and programmed cell death.

(a) Schematic diagram depicting the workflow opted to narrow down on the single metabolic gene mutants. **(b)** Screenshot of the central yeast metabolism from the Kyoto Encyclopedia of Genes and Genomes (KEGG) indicating the key metabolic pathways (highlighted in red) harboring metabolic intermediates predicted as high-affinity binders of GPCR-Gα-protein (Ste2p-Gpa1p) interface by Gcoupler. **(c)** Schematic diagram depicting the experimental design used to screen single metabolic gene mutants for α-factor-induced programmed cell death. Cell viability was assessed using Propidium iodide-based fluorometric assay. **(d)** Scatter plot depicting the impact of α-factor stimuli on cellular viability, assessed using Propidium iodide-based fluorometric assay. The y-axis represents $-\log_{10}$(p-value) of the one-sample student's t-test between the normalized PI fluorescence of untreated and treated conditions. The x-axis represents the percentage inhibition or increase in cellular viability, estimated using a Propidium Iodide-based assay. The mutants reported to be involved in mating, apoptosis, or both are indicated in orange, green, and blue, respectively. The statistically non-significant mutants are indicated below the dashed line in black. **(e)** Schematic diagram depicting the experimental workflow of the untargeted metabolomics experiment. Notably, the experiment involves the usage of increasing doses of α-factor to induce programmed cell death and to enrich the survival cells selectively. **(f)** Heatmap depicting the relative enrichment/de-enrichment of differentially enriched metabolites in the indicated conditions. Of note, four biological replicates per condition were used in the untargeted metabolomics. **(g)** Venn diagram depicting the overlap between the predicted endogenous intracellular allosteric modulators of Ste2p and differentially enriched metabolites (DEMs) identified using untargeted metabolomics. **(h)** Mean-whisker plot depicting the relative abundance of ubiquinone 6 (CoQ6) in the indicated conditions. Student's t-test was used to compute statistical significance. Asterisks indicate statistical significance, whereas ns represents non-significance. **(i)** Mean-whisker plot depicting the relative abundance of zymosterol (ZST) in the indicated conditions. Student's t-test was used to compute statistical significance. Asterisks indicate statistical significance, whereas ns represents non-significance.

Figure 4: Exogenous metabolites treatment resists α-factor-induced programmed cell death.

(a) Schematic diagram (left) depicting the workflow opted to monitor α-factor-induced programmed cell death in the wild-type yeast cells pre-loaded for 24 hours with ubiquinone 6 (CoQ6), zymosterol (ZST), and lanosterol (LST) at three different concentrations. Changes in the programmed cell death were quantified using the area under the curve (AUC) of the growth kinetics with respect to their respective controls. The box plot on the right depicts the rescue from the α-factor-induced programmed cell death in the indicated conditions (n=8 or 9 biological replicates). The y-axis represents the fold change of the AUC values with respect to their respective controls. Mann Whitney U test was used to calculate statistical significance. Asterisks indicate statistical significance, whereas ns represents non-significance. **(b)** The schematic diagram depicting the experimental workflow used to quantify α-factor-induced programmed cell death using a propidium iodide-based cell viability fluorometric assay. **(c)** Box plot depicting the rescue from the α-factor-induced programmed cell death in the indicated conditions as inferred using propidium iodide-based cell viability fluorometric assay (n=9 or 10 biological replicates; Heatkilled = 2). The y-axis represents the fold change of the propidium iodide fluorescence values with respect to their respective controls. Mann Whitney U test was used to calculate statistical significance. Asterisks indicate statistical significance, whereas ns represents non-significance. **(d)** Schematic representation (left) of the experimental approach used to measure cell vitality and viability using microscopy-based FUN^{TM}1 staining. Representative micrographs (right) depicting the FUN^{TM}1 staining results in the indicated conditions, Scale 10 µm. **(e)** Mean-whisker plot depicting the relative proportion of the vital and viable yeast cells observed using FUN^{TM}1 staining in the indicated conditions (n = 3 biological replicates). A Student's t-test was used to compute statistical significance. Asterisks indicate statistical significance, whereas ns represents non-significance. Error bars represent the standard error of the mean (SEM). **(f)** Schematic representation (left) of the experimental design for the mating assay (n = 3 biological replicates, each with three technical replicates). MATa yeast cells were pre-loaded with the metabolites and then mated with MATα cells to evaluate the mating efficiency. Representative micrographs in the middle qualitatively depict the mating efficiency in the indicated conditions. The bar plots on the right depict the mating efficiency (mean ± SEM) in the indicated conditions. Student's t-test was used to compute statistical significance. Asterisks indicate statistical significance, whereas ns represents non-significance. **(g)** Workflow depicting the steps involved in the molecular dynamics simulation of the Ste2p-metabolite docked complex using the AMBER software suite. **(h)** Barplots depicting the binding energies obtained by the docking of Ste2p and indicated metabolites across IC4 and IC5. **(i)** Line plot depicting the Root Mean Square Deviation (RMSD) changes over simulation timeframes from the three independent replicates of the indicated

conditions. The spread of the data is indicated as Standard Deviation (SD). Notably, RMSD is provided in Angstroms (Å), whereas the simulation time is in nanoseconds (ns).

Figure 5: Intracellular GPCR Allosteric-modulating metabolites attenuate Isoprotenol-mediated Hypertrophy Response.

(a) Workflow depicting the steps involved in Ste2p-miniG-protein docking using HADDOCK and PRODIGY web servers. **(b)** Barplots depicting the fold change of the dissociation constant (K_d) in the indicated conditions. Notably, fold change was computed with respect to the wild-type condition (Ste2p-miniG-protein). Inlets represent molecular representations of Ste2p-miniG-protein and the highlighted interface residues. **(c)** Workflow depicting the steps involved in Ste2p-miniG-protein docking of the wild-type and site-directed Ste2p mutants. Notably, docking was performed using HADDOCK and PRODIGY web servers. **(d)** Barplots depicting the dissociation constant (K_d) fold change in Ste2p site-directed mutants and wild-type. Notably, fold change was computed with respect to the wild-type condition (Ste2p-miniG-protein). **(e)** Schematic representation depicting the experimental design of RNA sequencing, featuring treatment duration and the sequencing parameters. **(f)** Heatmap depicting the expression of differentially expressed genes in the indicated conditions. Notably, Control and LST represent yeast cells unloaded and pre-loaded with lanosterol, respectively. α-factor is represented as α, where plus and minus signs represent its presence and absence, respectively. **(g)** A table highlighting the key differentially expressed genes in the indicated conditions reported to be involved in regulating yeast apoptosis-like signaling or mating response. Arrowheads and their direction represent the direction of differential expression. **(h)** Schematic representation of the experimental workflow followed to deduce the impact of indicated metabolites treatment on isoproterenol (ISO)-induced, GPCR-mediated hypertrophy response in human (AC16) and neonatal rat cardiomyocytes. Notably, in the case of AC16 cells, Wheat germ agglutinin (WGA) was used to stain the cardiomyocytes, whereas, for neonatal cardiomyocytes, alpha-sarcomeric actinin staining was used. **(i)** Micrographs depicting the human (above; green colored) and neonatal rat (below; red colored) cardiomyocytes in the indicated conditions. Scale 50 µm. **(j)** Box plot depicting the surface area of human (AC16) and neonatal rat cardiomyocytes in the indicated conditions. Statistical significance of indicated metabolites with untreated control and isoproterenol-treated conditions are indicated in green and grey text, respectively. Mann Whitney U test with Bonferroni corrected p-values was used to compute statistical significance.

SUPPLEMENTARY FIGURE LEGENDS

Supplementary Figure 1: Development of Gcoupler package.

(a) Flowchart depicting the entire workflow used to compute and compare the runtime using AutoDock and Gcoupler. Of note, the three major modules of Gcoupler, i.e., Synthesizer, Authenticator, and Generator, are indicated alongside their key processes. **(b)** AUC-ROC curves depicting the optimal probability cutoff recommended by G-means and Youden J index algorithms, respectively. Notably, the optimal threshold is indicated by the black dot on the ROC curve. **(c)** Ribbon diagram depicting the structure of ADRA1A predicted structure using Alphafold (ID: AF-P35348). **(d)** Waterfall chart depicting the timestamp information about the key steps involved in AutoDock. Of note, time consumed at the indicated steps is mentioned in seconds and hours along the y-axis and above bars, respectively. **(e)** Waterfall chart depicting the timestamp information about the key steps involved in Gcoupler. Of note, time consumed at the indicated steps is mentioned in seconds and hours along the y-axis and above bars, respectively. **(f)** Bar plot depicting the comparison between the total time consumed by the AutoDock and Gcoupler to predict the binding of experimentally validated ligands for ADRA1A (AF-P35348). **(g)** Boxplot depicting the performance metrics of the 10-fold cross-validation of the training data obtained using Gcoupler. **(h)** Boxplot depicting the performance metrics of the 10-fold cross-validation of the testing data obtained using Gcoupler. **(i)** Scatterplot depicting the relationship between AutoDock computed binding energies and Gcoupler computed prediction probabilities of the experimentally validated ligands of ADRA1A protein.

Supplementary Figure 2: Benchmarking on Experimentally-validated GPCRs

(a) Bar graphs indicating the performance of the indicated models generated using Gcoupler workflow. Note the models are made for the experimentally elucidated orthosteric sites of the indicated GPCRs. **(b)** AUC-ROC curves of the finally selected model for each of the indicated GPCRs. Note: Experimentally validated active ligands and decoys were used in the testing dataset. **(c)** Bar graphs depicting the sensitivities and specificities of the indicated GPCRs with experimentally validated active ligands and reported decoys. **(d)** Molecular representation of the indicated GPCRs with highlighted experimentally validated intracellular allosteric cavity and ligand. **(e)** Bar graphs depicting the performance metrics of the indicated classification model generated using Gcoupler for the highlighted allosteric cavities of the indicated proteins. **(f)** The AUC-ROC curve indicates the model performance for classifying HABs and LABs. **(g)** Bar graphs indicating the prediction probabilities of the indicated ligands for each of the indicated experimentally validated ligands. **(h)** Heatmap depicting the

RMSD values obtained by comparing all the GPCR-Gα-protein interfaces of the available human GPCRs from the protein databank. **(i)** Heatmap depicting the RMSD values obtained by comparing the selected human GPCRs available in the protein databank.

Supplementary Figure 3: Ste2 protein cavities prediction using Gcoupler

(a) Flowchart depicting the key steps used for the molecular dynamics simulation of the Ste2p using CHARMM-GUI and GROMACS software. **(b)** Line plot depicting the changes in the density (kg/m^3) along the z-axis of the three-dimensional Ste2p structure. **(c)** Line plot depicting the decline in the potential (kJ/mol) over molecular dynamics simulation time in picoseconds (ps). **(d)** Line plot depicting the changes in the density (kg/m^3) of the overall system over molecular dynamics simulation time in picoseconds (ps). **(e)** Line plots depicting the changes in the pressure (in bars) and temperature (in Kelvin) of the overall system during molecular dynamics simulation of Ste2 protein. **(f)** Line plot depicting the Root Mean Square Deviation (RMSD) changes of the Ste2 protein during molecular dynamics simulation. Note the RMSD values are indicated in nanometers (nm). **(g)** Ramachandran plot depicting the location of simulated Ste2 protein residues in the favorable and unfavorable regions. **(h)** Barplot depicting the predicted cavities volumes (Å). **(i)** Scatterplot depicting the relationship between the cavity volume and surface area in the indicated cavities of the Ste2 protein. **(j)** Heatmap depicting the percentage of amino acids of the indicated cavities residing in the EC (extracellular), IC (intracellular), and TM (transmembrane) region of the Ste2 protein. **(k)** Scatterplot depicting the predicted drug score of the indicated cavities of the Ste2 protein. **(l)** Snake plot depicting the conservation of Ste2 protein at the amino acid levels. Of note, Ste2 proteins from 15 related yeast species were used for computing the conservation score. **(m)** Snake plot depicting the key amino acids of the Ste2 protein alongside their location within the indicated functional cavities. **(n)** Heatmap illustrating the relative enrichment of the indicated functional groups (RNH2: primary amine, R2NH: secondary amine, R3N: tertiary amine, ROPO3: monophosphate, ROH: alcohol, RCHO: aldehyde, RCOR: ketone, RCOOH: carboxylic acid, RCOOR: ester, ROR: ether, RCCH: terminal alkyne, RCN: nitrile) among the Gcoupler-based *de novo* synthesized binders of Ste2p receptor across IC4 and IC5. **(o)** Venn diagrams depicting the number of yeast metabolites from YMDB predicted to bind to the Ste2p-Gpa1p interface, predicted using Gcoupler and AutoDock. Of note, IC4 and IC5 represent intracellular cavities 4 and 5 of the Ste2 protein, respectively.

Supplementary Figure 4: Benchmarking of different Gcoupler Modules.

(a) Venn diagram depicting the number of overlapping amino acids constituting the Extracellular Cavity 1 (EC1), Intracellular Cavity 4 (IC4), and Intracellular Cavity 5 (IC5) of the Ste2p. **(b)** Two-dimensional and **(c)** three-dimensional Principal Component Analysis plots depicting the segregation of *in-silico* synthesized ligands for the indicated cavities via Gcoupler. Of note, atom pair fingerprints were used as features for this analysis. **(d)** Scatter plot depicting the relationship between the depth of the pharmacophore features and the neighboring grids. **(e)** Donut charts illustrating the properties of amino acids constituting the pharmacophore for each of the indicated cavities. **(f)** Two-dimensional and **(g)** three-dimensional Principal Component Analysis plots depicting the chemical properties of *in-silico* synthesized ligands from five independent runs on the IC4 of the Ste2p using the Gcoupler Synthesizer module. Of note, atom pair fingerprints were used as features for this analysis. **(h)** Heatmap depicting the Tanimoto Similarities scores between the generated compounds for IC4 of Ste2p across five independent runs using Gcoupler. **(i)** Box plots depicting the performance parameters of the indicated models generated using Gcoupler against the IC4 cavity of Ste2p. Note the training and testing datasets were generated randomly (5 iterations) from the *in-silico* synthesized ligands from Gcoupler.

Supplementary Figure 5: Gcoupler predicted the high-affinity endogenous intracellular allosteric modulators of Ste2 protein.

(a) Principal Component Analysis depicting chemical heterogeneity of synthetic compounds synthesized using Gcoupler across intracellular cavities (IC4 and IC5). Notably, the compounds were segregated into High-Affinity Binders (HAB) and Low-Affinity Binders (LAB) by the Authenticator module of the Gcoupler. **(b)** Heatmap depicting the chemical similarity of the *de novo* synthesized HAB (dark green) and LAB (light green) across intracellular cavities (IC4 and IC5) of the Ste2 protein. Tanimoto similarities were computed using Atomic fingerprints. **(c)** Box plots depicting the model's performances across the 10-fold cross-validation. The upper and lower box plots depict the performance metrics of models trained using the *de novo* ligands for intracellular cavities (IC4 and IC5), respectively, of the Ste2 protein. **(d)** Principal Component Analysis depicting chemical heterogeneity of endogenous yeast metabolites predicted to bind to the intracellular cavities (IC4 and IC5) of the Ste2 protein. Notably, the compounds were segregated into High-Affinity Metabolites (HAM) and Low-Affinity Metabolites (LAM) by the Generator module of the Gcoupler. **(e)** Percentage stacked barplot depicting the relative enrichment of the indicated functional groups of the High-Affinity Metabolites (HAM) and Low-Affinity Metabolites (LAM) across intracellular cavities (IC4 and IC5) of the Ste2 protein. **(f)** Scatter plots depicting the segregation of High/Low-Affinity Metabolites (HAM/LAM) (indicated in green and red) identified using

Gcoupler workflow with 100% training data. Of note, models trained on lesser training data size (25%, 50%, and 75% of HAB/LAB) severely failed to segregate High-Affinity Metabolites (HAM) and Low-Affinity Metabolites (LAM) (along Y-axis). X-axis represents the binding affinity calculated using IC4-specific docking using AutoDock. **(g)** Bar plots depicting the correlation values obtained between the Gcoupler prediction probabilities and AutoDock computed binding energies in the indicated data size. **(h)** Box plots depicting the distributions for binding energies of the High-Affinity Metabolites and Low-Affinity Metabolites computed using cavity-specific docking and full docking via Autodock for IC4 and IC5 of the Ste2p.

Supplementary Figure 6: Untargeted metabolomics and genetic screening suggest an interlink between metabolites and Ste2p-mediated Programmed Cell Death.

(a) Venn diagram depicting the percentage overlaps of the mating-related genes reported in the literature and those used in the screening. The *STE2* was the only common gene. **(b)** Heatmap depicting the growth curve profiles of the wild-type, single metabolic mutants, and *ste2Δ* under optimal growth conditions. **(c)** Boxplot depicting the increase in the propidium iodide fluorescence upon the increasing concentration of α-factor treatment. Heat-killed (HK), untreated, and vehicle (DMSO-treated) were used as controls, whereas the increasing concentration of α-factor survived wild-type cells was used as test conditions. Mann Whitney U test was used to calculate statistical significance. Asterisks indicate statistical significance, whereas ns represents non-significance. **(d)** Principal Component Analysis depicting the segregation of indicated samples based on their metabolomics profiles along the PC1, PC2, and PC3. **(e)** Correlation plot depicting Pearson's correlation of the metabolome of the indicated samples. **(f)** Heatmap depicting the relative enrichment of all the detected metabolites in the indicated condition. Heat-killed (HK), untreated, and vehicle (DMSO-treated) were used as controls, whereas the increasing concentration of α-factor survived wild-type cells was used as test conditions. **(g)** Venn diagram indicating that 38 predicted intracellular allosteric modulators of Ste2p were identified in the untargeted metabolomics profiling. **(h)** Scatterplot depicting the Pathway Over Representation Analysis (ORA) results of the differentially enriched metabolites (treated vs. vehicle control) identified using untargeted metabolomics.

Supplementary Figure 7: Exogenous supplementation of selective metabolites rescues α-factor-mediated Programmed Cell Death.

(a) Growth curve profiles of the wild-type (control), *ste2Δ,* and wild-type yeast pre-treated with the indicated metabolites. **(b)** Beanplots depicting the changes in the α-factor-mediated programmed cell death in the indicated conditions. Notably, cell viability was assessed by computing the area under the curve (AUC) of the growth kinetics. Mann Whitney U test was used to calculate statistical significance. Asterisks indicate statistical significance, whereas ns represents non-significance. **(c)** Beanplot depicting the fold change in the α-factor-mediated programmed cell death, assessed using the propidium iodide-mediated programmed cell death in the indicated conditions. Mann Whitney U test was used to calculate statistical significance. Asterisks indicate statistical significance, whereas ns represents non-significance. **(d)** Representative micrographs (left) depicting the growth of the cells (mating response) pretreated with indicated metabolites in a single drop-out medium (SC-Lys and SC-Met). Quantifications of the mating response are indicated as a bar graph (mean ± SEM) on the right (n = 3 biological replicates, each with three technical replicates). Student's t-test was used to compute statistical significance. Asterisks indicate statistical significance, whereas ns represents non-significance.

Supplementary Figure 8: Docking and Molecular Dynamics simulations suggest the stability of the Ste2-metabolite complex.

(a) Ligplots depicting the interacting amino acid residues and atoms of the Ste2 protein and indicated metabolites for the intracellular cavities (IC4 and IC5). **(b)** Table indicating the Van der Waals (ΔE_{vdw}), electrostatic (ΔE_{elec}), polar solvation (ΔE_{psolv}), and non-polar solvation (ΔE_{npsolv}) energies along with net binding free-energy (ΔG_{bind}) in kcal/mol of the three independent replicates of the indicated metabolites across intracellular cavities IC4 and IC5 of the Ste2p. Note the values in the table are provided as mean ± standard errors. **(c)** Line plots depicting the total energy decomposition of the individual amino acids of the Ste2p (three independent replicates) computed using MD simulations in IC4 (left) and IC5 (right).

Supplementary Figure 9: RNA-Sequencing unveils genes involved in attenuating α-factor-induced cell death response.

(a) Line plot depicting the variation in the RMSD of the indicated metabolites bound to the intracellular cavity 4 (IC4) at the GPCR-Gα interface of the Ste2p, obtained using longer MD simulation runs. Notably, RMSD is provided in Angstroms (Å), whereas the simulation time is in nanoseconds (ns). **(b)** Molecular representation of the Ste2 protein structures (blue) and the miniGpa1-proteins (cyan), with the highlighted interface residues (red and green) in the indicated conditions. **(c)** Scatterplot depicting the net binding free-energy ΔG (kcal/mol) of

the Ste2p (with and without indicated metabolites) with miniG-protein (y-axis) and α-factor (x-axis). **(d)** Barplot depicting RMSD values of the Ste2 protein with indicated metabolite across intracellular cavities IC4 and IC5. **(e)** Ligplots depicting the interacting amino acid residues of the mutant Ste2 proteins (mutation site indicated) and atoms of indicated metabolites at the intracellular cavities (IC4 and IC5). **(f)** M-D plots (left) from the NOIseq analysis highlight the differentially expressed genes (colored) in the indicated conditions. Bar plots (middle) depict the prominent Gene Ontologies in the indicated conditions. Venn diagram (right) depicting the overlaps between the differentially expressed genes and the genes used in biochemical assays in this study.

Supplementary Figure 10: Evolutionary Conservation of GPCR-Gα interface.
(a) Table depicting the conservation of yeast Ste2p-metabolite (ZST, CoQ6, and LST) interacting residues in the adrenergic receptors from humans and rats. **(b)** Molecular representations depicting the topology of human and rat ADRB1 and ADRB2 receptors. GPCR-Gα interface cavities are color-coded at the intracellular sites. Of note, in the case of human ADRB1, the nomenclature of the two cavities detected at the interface includes 'Cv' (cavity) succeeded by the numerical number. **(c)** Barplots depicting the binding energies obtained by the docking of Human ADRB1 (7BVQ), Human ADRB2 (5X7D), Rat ADRB1 (P18090), and Rat ADRB2 (P10608) with the indicated metabolites at the GPCR-Gα interfaces.

SUPPLEMENTARY DATA

Supplementary Table 1: Table contains information about the structure of the human GPCR-Gα-Protein complexes downloaded from the Protein Data Bank (PDB). It also contains information about the PDB IDs, Protein name, species information, whether it is used in this study or not, UniProt IDs, and other information.

Supplementary Table 2: The table contains information about the normalized Root Mean Square Deviation (RMSD) of the pairwise comparison of the GPCR-Gα-Protein interface (cavities) for the indicated GPCRs.

Supplementary Table 3: The table contains information about the chemical similarities of the *de novo* synthesized synthetic compounds of the indicated GPCR-Gα-Protein interface

(cavities). Of note, the chemical similarity was computed using the Taniomoto coefficient on the Atomic fingerprints.

Supplementary Table 4: The table contains information about the YMDB metabolites predicted to bind at the intracellular cavities IC4 and IC5 of the Ste2 protein. Of note, predictions were made using molecular docking and Gcoupler. It contains information about the YMDB ID, Metabolite name, SMILES (Simplified Molecular Input Line Entry System), and cavities information. Of note, BE refers to binding energies, whereas probabilities were the outcome of Gcoupler.

Supplementary Table 5: The table contains information about the list of metabolite-gene pairs from the Kyoto Encyclopedia of Genes and Genomes (KEGG) pathway that is used in this study.

Supplementary Table 6: The table contains the results of the untargeted metabolomics. Of note, the values represent normalized and imputed peak intensities of the indicated metabolites.

Supplementary Table 7: The table contains information about the known mutants from the literature that could modulate Ste2 signaling. Of note, the table also contains information about the site of mutation, the nature of the mutation, its position within the intracellular cavities IC4 and IC5, their impact on the Ste2 signaling pathway, and references.

Supplementary Table 8: The table contains the TMM normalized read counts after RNA Sequencing.

Supplementary Table 9: The table contains the list of Differentially Expressed Genes (DEGs) of the Control groups, alongside the other standard output from the NOISeq analysis, such as M and D values, mean values of the two conditions, probability ranking, and other gene-associated features.

Supplementary Table 10: The table contains the list of Differentially Expressed Genes (DEGs) of the Control-LST group, alongside the other standard output from the NOISeq analysis, such as M and D values, mean values of the two conditions, probability ranking, and other gene-associated features.

Supplementary Table 11: The table contains the list of Differentially Expressed Genes (DEGs) of the LST group, alongside the other standard output from the NOISeq analysis, such as M and D values, mean values of the two conditions, probability ranking, and other gene-associated features.

REFERENCES

1. Yang, D. *et al.* G protein-coupled receptors: structure- and function-based drug discovery. *Signal Transduction and Targeted Therapy* **6**, 1–27 (2021).
2. Alhosaini, K., Azhar, A., Alonazi, A. & Al-Zoghaibi, F. GPCRs: The most promiscuous druggable receptor of the mankind. *Saudi Pharmaceutical Journal* **29**, 539–551 (2021).
3. Calebiro, D., Koszegi, Z., Lanoiselée, Y., Miljus, T. & O'Brien, S. G protein-coupled receptor-G protein interactions: a single-molecule perspective. *Physiol. Rev.* **101**, 857–906 (2021).
4. Wold, E. A. & Zhou, J. GPCR Allosteric Modulators: Mechanistic Advantages and Therapeutic Applications. *Curr. Top. Med. Chem.* **18**, 2002–2006 (2018).
5. Bourque, K. *et al.* Exploring the use of intracellular and extracellular allosteric

modulators to understand GPCR signaling. *Allosteric Modulation of G Protein-Coupled Receptors* 135–160 Preprint at https://doi.org/10.1016/b978-0-12-819771-4.00008-7 (2022).

6. Rees, S., Morrow, D. & Kenakin, T. GPCR Drug Discovery Through the Exploitation of Allosteric Drug Binding Sites. *Receptors and Channels* vol. 8 261–268 Preprint at https://doi.org/10.3109/10606820214640 (2002).
7. Leach, K., Sexton, P. M. & Christopoulos, A. Allosteric GPCR modulators: taking advantage of permissive receptor pharmacology. *Trends Pharmacol. Sci.* **28**, 382–389 (2007).
8. van der Westhuizen, E. T., Valant, C., Sexton, P. M. & Christopoulos, A. Endogenous Allosteric Modulators of G Protein–Coupled Receptors. *J. Pharmacol. Exp. Ther.* **353**, 246–260 (2015).
9. Stornaiuolo, M. *et al.* Endogenous vs Exogenous Allosteric Modulators in GPCRs: A dispute for shuttling CB1 among different membrane microenvironments. *Sci. Rep.* **5**, 15453 (2015).
10. Doller, D. Endogenous Allosteric Modulators of G Protein-Coupled Receptors: Implications in Drug Design. *2017 Medicinal Chemistry Reviews* 343–360 Preprint at https://doi.org/10.29200/acsmedchemrev-v52.ch18 (2017).
11. Reyes-Alcaraz, A., Lucero Garcia-Rojas, E. Y., Bond, R. A. & McConnell, B. K. Allosteric Modulators for GPCRs as a Therapeutic Alternative with High Potential in Drug Discovery. *Molecular Pharmacology* Preprint at https://doi.org/10.5772/intechopen.91838 (2020).
12. Zhang, P., Covic, L. & Kuliopulos, A. Pepducins and Other Lipidated Peptides as Mechanistic Probes and Therapeutics. *Methods Mol. Biol.* **1324**, 191–203 (2015).
13. O'Callaghan, K., Kuliopulos, A. & Covic, L. Turning receptors on and off with intracellular pepducins: new insights into G-protein-coupled receptor drug development. *J. Biol. Chem.* **287**, 12787–12796 (2012).
14. Basith, S. *et al.* Exploring G Protein-Coupled Receptors (GPCRs) Ligand Space via

Cheminformatics Approaches: Impact on Rational Drug Design. *Front. Pharmacol.* **9**, 128 (2018).

15. Gupta, A. *et al.* Machine-OlF-Action: A unified framework for developing and interpreting machine-learning models for chemosensory research. *Bioinformatics* (2021) doi:10.1093/bioinformatics/btaa1104.
16. Zhou, Y., Meng, J., Xu, C. & Liu, J. Multiple GPCR Functional Assays Based on Resonance Energy Transfer Sensors. *Front Cell Dev Biol* **9**, 611443 (2021).
17. Hoffmann, C. & Bünemann, M. Fluorescence and Resonance Energy Transfer Shine New Light on GPCR Function. *GPCR Molecular Pharmacology and Drug Targeting* 226–251 Preprint at https://doi.org/10.1002/9780470627327.ch10 (2010).
18. Jaeger, W. C., Pfleger, K. D. G. & Eidne, K. A. Monitoring GPCR-Protein Complexes Using Bioluminescence Resonance Energy Transfer. *G Protein-Coupled Receptors* 111–132 Preprint at https://doi.org/10.1002/9780470749210.ch6.
19. Congreve, M., de Graaf, C., Swain, N. A. & Tate, C. G. Impact of GPCR Structures on Drug Discovery. *Cell* **181**, 81–91 (2020).
20. Topiol, S. Current and Future Challenges in GPCR Drug Discovery. *Methods Mol. Biol.* **1705**, 1–21 (2018).
21. Spiegel, J. O. & Durrant, J. D. AutoGrow4: an open-source genetic algorithm for de novo drug design and lead optimization. *J. Cheminform.* **12**, 25 (2020).
22. Sicho, M., Liu, X., Svozil, D. & van Westen, G. J. P. GenUI: interactive and extensible open source software platform for de novo molecular generation and cheminformatics. *J. Cheminform.* **13**, 73 (2021).
23. Li, Y., Pei, J. & Lai, L. Structure-based de novo drug design using 3D deep generative models. *Chem. Sci.* **12**, 13664–13675 (2021).
24. Böhm, H. J. The computer program LUDI: a new method for the de novo design of enzyme inhibitors. *J. Comput. Aided Mol. Des.* **6**, 61–78 (1992).
25. Nishibata, Y. & Itai, A. Automatic creation of drug candidate structures based on receptor structure. Starting point for artificial lead generation. *Tetrahedron* **47**, 8985–

8990 (1991).

26. Pearlman, D. A. & Murcko, M. A. CONCEPTS: New dynamic algorithm forde novo drug suggestion. *J. Comput. Chem.* **14**, 1184–1193 (1993).
27. Yuan, Y., Pei, J. & Lai, L. LigBuilder 2: a practical de novo drug design approach. *J. Chem. Inf. Model.* **51**, 1083–1091 (2011).
28. Nakayama, N., Kaziro, Y., Arai, K. & Matsumoto, K. Role of STE genes in the mating factor signaling pathway mediated by GPA1 in Saccharomyces cerevisiae. *Mol. Cell. Biol.* **8**, 3777–3783 (1988).
29. Alvaro, C. G. & Thorner, J. Heterotrimeric G Protein-coupled Receptor Signaling in Yeast Mating Pheromone Response. *J. Biol. Chem.* **291**, 7788–7795 (2016).
30. Blumer, K. J., Reneke, J. E. & Thorner, J. The STE2 gene product is the ligand-binding component of the alpha-factor receptor of Saccharomyces cerevisiae. *J. Biol. Chem.* **263**, 10836–10842 (1988).
31. Büttner, S. *et al.* Why yeast cells can undergo apoptosis: death in times of peace, love, and war. *J. Cell Biol.* **175**, 521–525 (2006).
32. Severin, F. F. & Hyman, A. A. Pheromone induces programmed cell death in S. cerevisiae. *Curr. Biol.* **12**, R233–5 (2002).
33. Zhang, N.-N. *et al.* Multiple signaling pathways regulate yeast cell death during the response to mating pheromones. *Mol. Biol. Cell* **17**, 3409–3422 (2006).
34. Carmona-Gutierrez, D. *et al.* Apoptosis in yeast: triggers, pathways, subroutines. *Cell Death Differ.* **17**, 763–773 (2010).
35. Sokolov, S. S., Galkina, K. V., Litvinova, E. A., Knorre, D. A. & Severin, F. F. The Role of LAM Genes in the Pheromone-Induced Cell Death of S. cerevisiae Yeast. *Biochemistry* **85**, 300–309 (2020).
36. Nadal-Ribelles, M. *et al.* Sensitive high-throughput single-cell RNA-seq reveals within-clonal transcript correlations in yeast populations. *Nat Microbiol* **4**, 683–692 (2019).
37. Hughes, J. P., Rees, S., Kalindjian, S. B. & Philpott, K. L. Principles of early drug discovery. *Br. J. Pharmacol.* **162**, 1239–1249 (2011).

38. Schöneberg, T., Hofreiter, M., Schulz, A. & Römpler, H. Learning from the past: evolution of GPCR functions. *Trends Pharmacol. Sci.* **28**, 117–121 (2007).

39. Magalhaes, A. C., Dunn, H. & Ferguson, S. S. Regulation of GPCR activity, trafficking and localization by GPCR-interacting proteins. *Br. J. Pharmacol.* **165**, 1717–1736 (2012).

40. Hedderich, J. B. *et al.* The pocketome of G-protein-coupled receptors reveals previously untargeted allosteric sites. *Nat. Commun.* **13**, 2567 (2022).

41. Yuan, Y., Pei, J. & Lai, L. LigBuilder V3: A Multi-Target de novo Drug Design Approach. *Front Chem* **8**, 142 (2020).

42. Berger, V. W. & Zhou, Y. Kolmogorov–Smirnov Test: Overview. *Wiley StatsRef: Statistics Reference Online* Preprint at https://doi.org/10.1002/9781118445112.stat06558 (2014).

43. Goerg, S. J. & Kaiser, J. Nonparametric Testing of Distributions—the Epps–Singleton Two-Sample Test using the Empirical Characteristic Function. *Stata J.* **9**, 454–465 (2009).

44. Engmann, S. & Cousineau, D. Comparing distributions: the two-sample Anderson-Darling test as an alternative to the Kolmogorov-Smirnoff test. *Journal of applied quantitative methods* **6**, (2011).

45. Mysinger, M. M., Carchia, M., Irwin, J. J. & Shoichet, B. K. Directory of useful decoys, enhanced (DUD-E): better ligands and decoys for better benchmarking. *J. Med. Chem.* **55**, 6582–6594 (2012).

46. Ramsundar, B. *et al.* DeepChem: Democratizing Deep-Learning for Drug Discovery, Quantum Chemistry. *Materials Science and Biology. https://github. com/deepchem/deepchem (accessed Aug 8, 2017)* (2019).

47. Shen, S. *et al.* Allosteric modulation of G protein-coupled receptor signaling. *Front. Endocrinol.* **14**, 1137604 (2023).

48. Morris, G. M. *et al.* AutoDock4 and AutoDockTools4: Automated docking with selective receptor flexibility. *J. Comput. Chem.* **30**, 2785–2791 (2009).

49. Gaulton, A. *et al.* ChEMBL: a large-scale bioactivity database for drug discovery. *Nucleic Acids Res.* **40**, D1100–7 (2012).

50. Liao, Z. *et al.* DeepDock: Enhancing Ligand-protein Interaction Prediction by a Combination of Ligand and Structure Information. in *2019 IEEE International Conference on Bioinformatics and Biomedicine (BIBM)* 311–317 (2019).

51. Gentile, F. *et al.* Deep Docking: A Deep Learning Platform for Augmentation of Structure Based Drug Discovery. *ACS Cent. Sci.* **6**, 939–949 (2020).

52. Gentile, F. *et al.* Artificial intelligence–enabled virtual screening of ultra-large chemical libraries with deep docking. *Nat. Protoc.* **17**, 672–697 (2022).

53. Jewison, T. *et al.* YMDB: the Yeast Metabolome Database. *Nucleic Acids Res.* **40**, D815–20 (2012).

54. Velazhahan, V. *et al.* Structure of the class D GPCR Ste2 dimer coupled to two G proteins. *Nature* **589**, 148–153 (2021).

55. Kaneko, H., Hosohara, M., Tanaka, M. & Itoh, T. Lipid composition of 30 species of yeast. *Lipids* **11**, 837–844 (1976).

56. Chong, J. *et al.* MetaboAnalyst 4.0: towards more transparent and integrative metabolomics analysis. *Nucleic Acids Res.* **46**, W486–W494 (2018).

57. Kanehisa, M. & Goto, S. KEGG: kyoto encyclopedia of genes and genomes. *Nucleic Acids Res.* **28**, 27–30 (2000).

58. Caspi, R. *et al.* The MetaCyc database of metabolic pathways and enzymes and the BioCyc collection of pathway/genome databases. *Nucleic Acids Res.* **44**, D471–80 (2016).

59. Van Zandycke, S. M., Simal, O., Gualdoni, S. & Smart, K. A. Determination of Yeast Viability Using Fluorophores. *J. Am. Soc. Brew. Chem.* **61**, 15–22 (2003).

60. Teng, X. & Hardwick, J. M. Reliable method for detection of programmed cell death in yeast. *Methods Mol. Biol.* **559**, 335–342 (2009).

61. Guedes, J. P. *et al.* Acetic acid triggers cytochrome c release in yeast heterologously expressing human Bax. *Apoptosis* **27**, 368–381 (2022).

62. Martins, V. M. *et al.* Contacts in Death: The Role of the ER-Mitochondria Axis in Acetic Acid-Induced Apoptosis in Yeast. *J. Mol. Biol.* **431**, 273–288 (2019).

63. Bardwell, L. A walk-through of the yeast mating pheromone response pathway. *Peptides* **26**, 339–350 (2005).

64. Hartwell, L. H. Mutants of Saccharomyces cerevisiae unresponsive to cell division control by polypeptide mating hormone. *J. Cell Biol.* **85**, 811–822 (1980).

65. Nachtergaele, S. *et al.* Oxysterols are allosteric activators of the oncoprotein Smoothened. *Nat. Chem. Biol.* **8**, 211–220 (2012).

66. Chatzigoulas, A. & Cournia, Z. Rational design of allosteric modulators: Challenges and successes. *Wiley Interdiscip. Rev. Comput. Mol. Sci.* **11**, (2021).

67. Bartuzi, D., Kaczor, A. A. & Matosiuk, D. Opportunities and Challenges in the Discovery of Allosteric Modulators of GPCRs. *Methods Mol. Biol.* **1705**, 297–319 (2018).

68. Hou, T., Bian, Y., McGuire, T. & Xie, X.-Q. Integrated Multi-Class Classification and Prediction of GPCR Allosteric Modulators by Machine Learning Intelligence. *Biomolecules* **11**, (2021).

69. Topiol, S. New opportunities for GPCR allosteric modulators. *Future Medicinal Chemistry* vol. 10 707–710 Preprint at https://doi.org/10.4155/fmc-2017-0313 (2018).

70. Horn, F. *et al.* GPCRDB information system for G protein-coupled receptors. *Nucleic Acids Res.* **31**, 294–297 (2003).

71. Bagnat, M. & Simons, K. Cell surface polarization during yeast mating. *Proc. Natl. Acad. Sci. U. S. A.* **99**, 14183–14188 (2002).

72. Jin, H., McCaffery, J. M. & Grote, E. Ergosterol promotes pheromone signaling and plasma membrane fusion in mating yeast. *J. Cell Biol.* **180**, 813–826 (2008).

73. Heese-Peck, A. *et al.* Multiple functions of sterols in yeast endocytosis. *Mol. Biol. Cell* **13**, 2664–2680 (2002).

74. Aguilar, P. S. *et al.* Structure of sterol aliphatic chains affects yeast cell shape and cell fusion during mating. *Proceedings of the National Academy of Sciences* **107**, 4170–4175 (2010).

75. Tiedje, C., Holland, D. G., Just, U. & Höfken, T. Proteins involved in sterol synthesis interact with Ste20 and regulate cell polarity. *J. Cell Sci.* **120**, 3613–3624 (2007).

76. Shaw, W. M. *et al.* Engineering a Model Cell for Rational Tuning of GPCR Signaling. *Cell* **177**, 782–796.e27 (2019).

77. Ostrov, N. *et al.* A modular yeast biosensor for low-cost point-of-care pathogen detection. *Sci Adv* **3**, e1603221 (2017).

78. Johnston, E. J., Moses, T. & Rosser, S. J. The wide-ranging phenotypes of ergosterol biosynthesis mutants, and implications for microbial cell factories. *Yeast* **37**, 27–44 (2020).

79. Clark, M., Cramer, R. D. & Van Opdenbosch, N. Validation of the general purpose tripos 5.2 force field. *J. Comput. Chem.* **10**, 982–1012 (1989).

80. Trott, O. & Olson, A. J. AutoDock Vina: improving the speed and accuracy of docking with a new scoring function, efficient optimization, and multithreading. *J. Comput. Chem.* **31**, 455–461 (2010).

81. Landrum, G. RDKit: A software suite for cheminformatics, computational chemistry, and predictive modeling. http://www.rdkit.org/RDKit_Overview.pdf.

82. Kipf, T. N. & Welling, M. Semi-Supervised Classification with Graph Convolutional Networks. *arXiv [cs.LG]* (2016).

83. Xiong, Z. *et al.* Pushing the Boundaries of Molecular Representation for Drug Discovery with the Graph Attention Mechanism. *J. Med. Chem.* **63**, 8749–8760 (2020).

84. Veličković, P. *et al.* Graph Attention Networks. *https://openreview.net › forumhttps://openreview.net › forum* (2018).

85. Jumper, J. *et al.* Highly accurate protein structure prediction with AlphaFold. *Nature* **596**, 583–589 (2021).

86. O'Boyle, N. M. *et al.* Open Babel: An open chemical toolbox. *J. Cheminform.* **3**, 33 (2011).

87. Dallakyan, S. MGLTools. *Reference Source*.

88. Edgar, R. C. MUSCLE: multiple sequence alignment with high accuracy and high

throughput. *Nucleic Acids Res.* **32**, 1792–1797 (2004).

89. Battle, G. M. PDBePISA: Identifying and interpreting the likely biological assemblies of a protein structure. *Chemistry*.
90. Moriwaki, H., Tian, Y.-S., Kawashita, N. & Takagi, T. Mordred: a molecular descriptor calculator. *J. Cheminform.* **10**, 4 (2018).
91. Abraham, M. J. *et al.* GROMACS: High performance molecular simulations through multi-level parallelism from laptops to supercomputers. *SoftwareX* **1-2**, 19–25 (2015).
92. Case, D. A. *et al.* The Amber biomolecular simulation programs. *J. Comput. Chem.* **26**, 1668–1688 (2005).
93. Jo, S., Kim, T., Iyer, V. G. & Im, W. CHARMM-GUI: a web-based graphical user interface for CHARMM. *J. Comput. Chem.* **29**, 1859–1865 (2008).
94. Sprenger, K. G., Jaeger, V. W. & Pfaendtner, J. The general AMBER force field (GAFF) can accurately predict thermodynamic and transport properties of many ionic liquids. *J. Phys. Chem. B* **119**, 5882–5895 (2015).
95. Tian, C. *et al.* ff19SB: Amino-Acid-Specific Protein Backbone Parameters Trained against Quantum Mechanics Energy Surfaces in Solution. *J. Chem. Theory Comput.* **16**, 528–552 (2020).
96. Wang, H. & Yang, W. Force Field for Water Based on Neural Network. *J. Phys. Chem. Lett.* **9**, 3232–3240 (2018).
97. van Zundert, G. C. P. *et al.* The HADDOCK2.2 Web Server: User-Friendly Integrative Modeling of Biomolecular Complexes. *J. Mol. Biol.* **428**, 720–725 (2016).
98. Xue, L. C., Rodrigues, J. P., Kastritis, P. L., Bonvin, A. M. & Vangone, A. PRODIGY: a web server for predicting the binding affinity of protein-protein complexes. *Bioinformatics* **32**, 3676–3678 (2016).
99. Mittal, A. *et al.* Artificial intelligence uncovers carcinogenic human metabolites. *Nat. Chem. Biol.* (2022) doi:10.1038/s41589-022-01110-7.
100. Tarazona, S. *et al.* Data quality aware analysis of differential expression in RNA-seq with NOISeq R/Bioc package. *Nucleic Acids Res.* **43**, e140 (2015).

101. Hammer, Ø., Harper, D. A. T. & Ryan, P. D. PAST: Paleontological statistics software package for education and data analysis. *Palaeontol. Electronica* (2001).

102. Core Team, R. R: A language and environment for statistical computing. Version 3.6. 0. Vienna, Austria. */ra-language-and-environment-forstatistical-computing*.

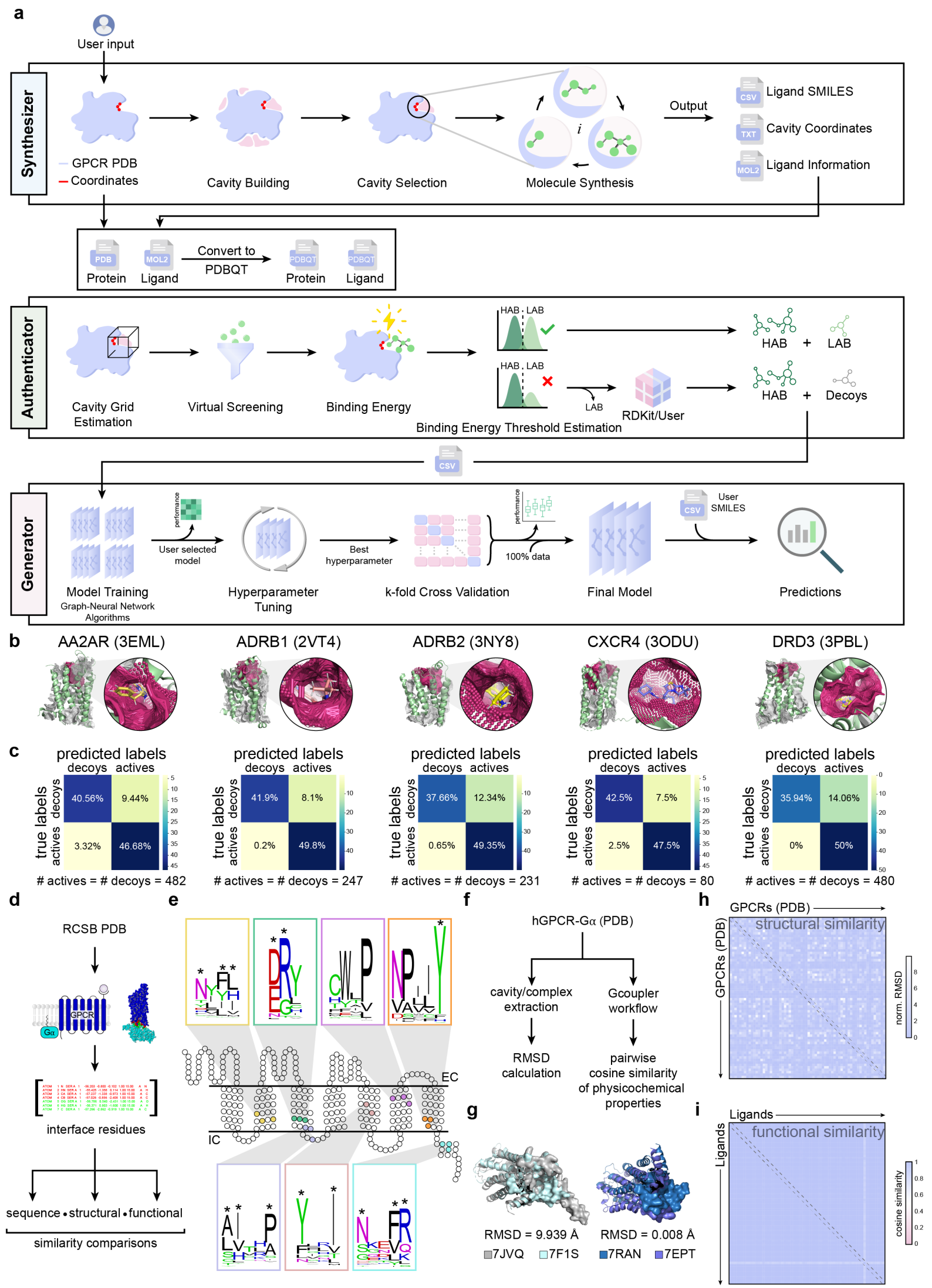
a
User input
Synthesizer
GPCR PDB
Coordinates
Cavity Building
Cavity Selection
Molecule Synthesis
Output
Ligand SMILES
Cavity Coordinates
Ligand Information
Protein
Ligand
Convert to PDBQT
Protein
Ligand
Authenticator
Cavity Grid Estimation
Virtual Screening
Binding Energy
HAB
LAB
HAB + LAB
HAB + Decoys
RDKit/User
Binding Energy Threshold Estimation
Generator
Model Training
Graph-Neural Network Algorithms
User selected model
Hyperparameter Tuning
Best hyperparameter
k-fold Cross Validation
100% data
Final Model
User SMILES
Predictions
b
AA2AR (3EML)
ADRB1 (2VT4)
ADRB2 (3NY8)
CXCR4 (3ODU)
DRD3 (3PBL)
c
predicted labels
decoys actives
true labels
40.56% 9.44%
3.32% 46.68%
actives = # decoys = 482
41.9% 8.1%
0.2% 49.8%
actives = # decoys = 247
37.66% 12.34%
0.65% 49.35%
actives = # decoys = 231
42.5% 7.5%
2.5% 47.5%
actives = # decoys = 80
35.94% 14.06%
0% 50%
actives = # decoys = 480
d
RCSB PDB
GPCR
Gα
interface residues
sequence • structural • functional
similarity comparisons
e
EC
IC
f
hGPCR-Gα (PDB)
cavity/complex extraction
Gcoupler workflow
RMSD calculation
pairwise cosine similarity of physicochemical properties
g
RMSD = 9.939 Å
RMSD = 0.008 Å
7JVQ
7F1S
7RAN
7EPT
h
GPCRs (PDB)
structural similarity
norm. RMSD
i
Ligands
functional similarity
cosine similarity

Figure 1

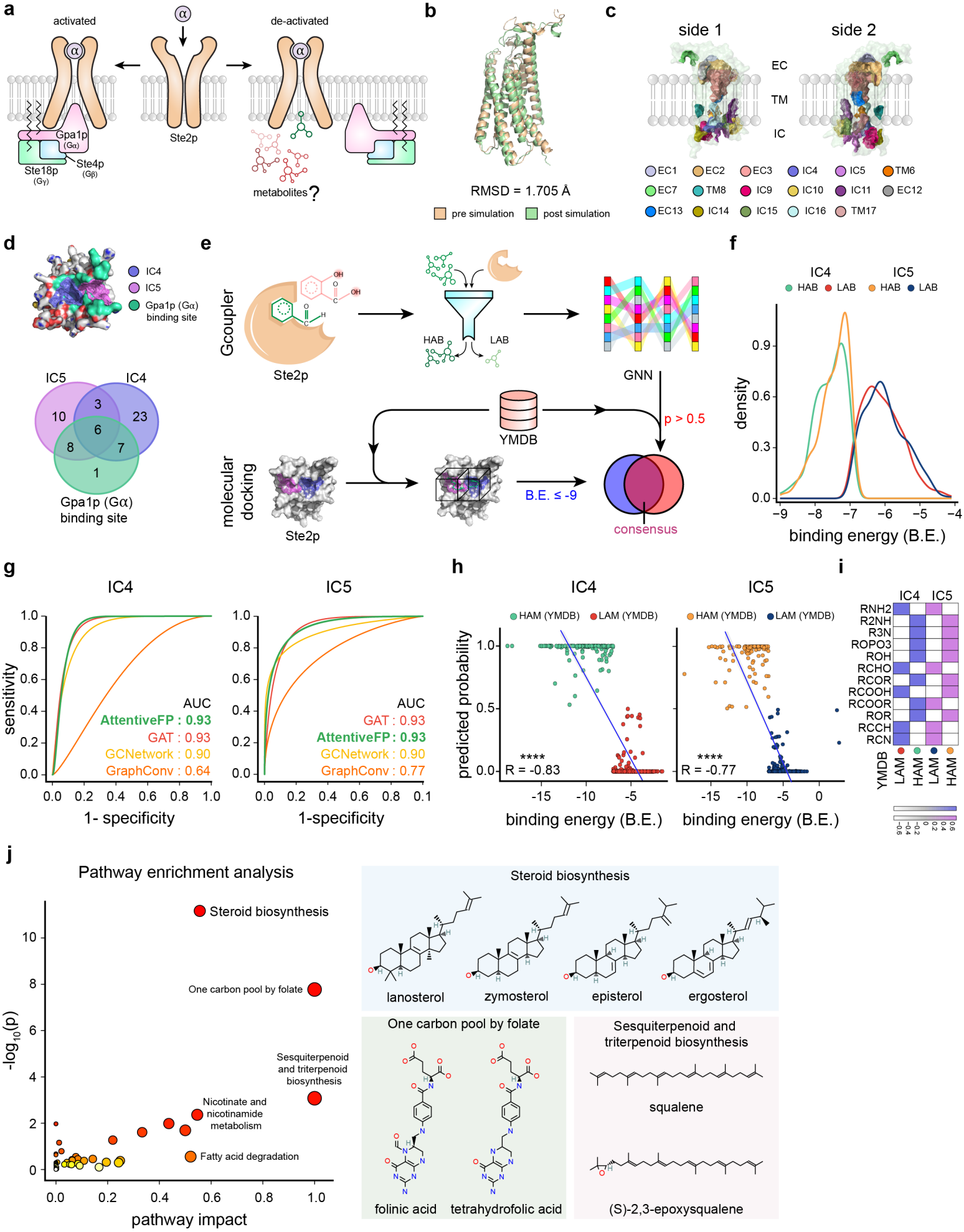
a
activated
de-activated
Ste2p
Gpa1p (Gα)
Ste18p (Gγ)
Ste4p (Gβ)
metabolites?
b
RMSD = 1.705 Å
pre simulation
post simulation
c
side 1
side 2
EC
TM
IC
EC1 EC2 EC3 IC4 IC5 TM6
EC7 TM8 IC9 IC10 IC11 EC12
EC13 IC14 IC15 IC16 TM17
d
IC4
IC5
Gpa1p (Gα) binding site
IC5 IC4
3 10 23 6 8 7 1
Gpa1p (Gα) binding site
e
Gcoupler
Ste2p
HAB
LAB
GNN
YMDB
p > 0.5
molecular docking
Ste2p
B.E. ≤ -9
consensus
f
IC4 IC5
HAB LAB HAB LAB
density
binding energy (B.E.)
g
IC4
IC5
sensitivity
1- specificity
AUC
AttentiveFP : 0.93
GAT : 0.93
GCNetwork : 0.90
GraphConv : 0.64
AUC
GAT : 0.93
AttentiveFP : 0.93
GCNetwork : 0.90
GraphConv : 0.77
h
IC4
IC5
HAM (YMDB) LAM (YMDB)
predicted probability
****
R = -0.83
R = -0.77
binding energy (B.E.)
i
IC4 IC5
RNH2
R2NH
R3N
ROPO3
ROH
RCHO
RCOR
RCOOH
RCOOR
ROR
RCCH
RCN
YMDB
LAM HAM LAM HAM
j
Pathway enrichment analysis
Steroid biosynthesis
One carbon pool by folate
Sesquiterpenoid and triterpenoid biosynthesis
Nicotinate and nicotinamide metabolism
Fatty acid degradation
-log10(p)
pathway impact
Steroid biosynthesis
lanosterol
zymosterol
episterol
ergosterol
One carbon pool by folate
folinic acid
tetrahydrofolic acid
Sesquiterpenoid and triterpenoid biosynthesis
squalene
(S)-2,3-epoxysqualene

Figure 2

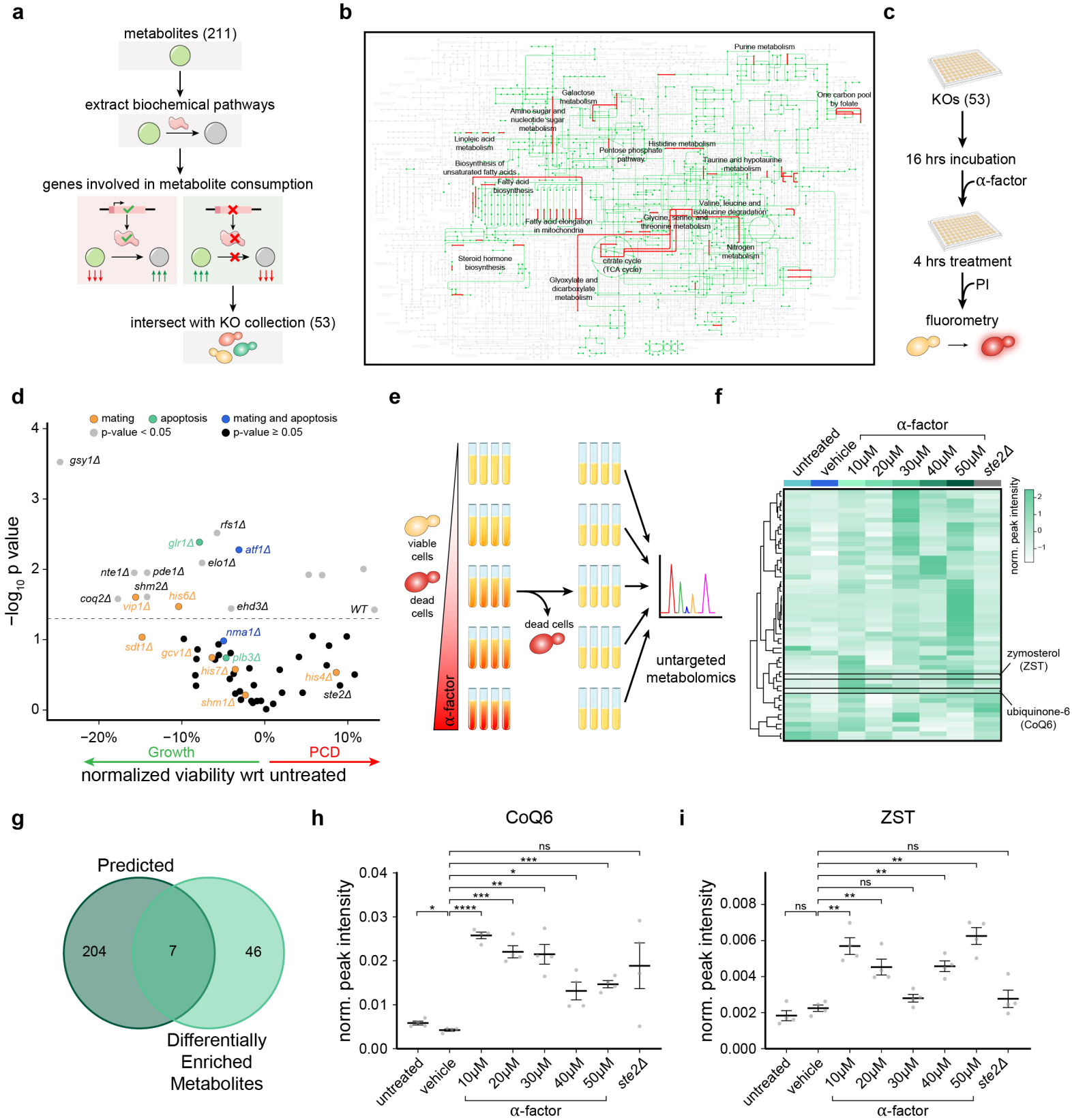
a
metabolites (211)
extract biochemical pathways
genes involved in metabolite consumption
intersect with KO collection (53)
b
Purine metabolism
Galactose metabolism
One carbon pool by folate
Amino sugar and nucleotide sugar metabolism
Linoleic acid metabolism
Histidine metabolism
Pentose phosphate pathway
Taurine and hypotaurine metabolism
Biosynthesis of unsaturated fatty acids
Fatty acid biosynthesis
Valine, leucine and isoleucine degradation
Fatty acid elongation in mitochondria
Glycine, serine, and threonine metabolism
Nitrogen metabolism
Steroid hormone biosynthesis
citrate cycle (TCA cycle)
Glyoxylate and dicarboxylate metabolism
c
KOs (53)
16 hrs incubation
α-factor
4 hrs treatment
PI
fluorometry
d
mating
apoptosis
mating and apoptosis
p-value < 0.05
p-value ≥ 0.05
−log10 p value
gsy1Δ
rfs1Δ
glr1Δ
atf1Δ
elo1Δ
nte1Δ
pde1Δ
shm2Δ
coq2Δ
his6Δ
vip1Δ
ehd3Δ
WT
nma1Δ
sdt1Δ
gcv1Δ
plb3Δ
his7Δ
his4Δ
ste2Δ
shm1Δ
−20%
−10%
0%
10%
Growth
PCD
normalized viability wrt untreated
e
viable cells
dead cells
α-factor
dead cells
untargeted metabolomics
f
α-factor
untreated
vehicle
10μM
20μM
30μM
40μM
50μM
ste2Δ
norm. peak intensity
zymosterol (ZST)
ubiquinone-6 (CoQ6)
g
Predicted
204
7
46
Differentially Enriched Metabolites
h
CoQ6
norm. peak intensity
untreated
vehicle
10μM
20μM
30μM
40μM
50μM
ste2Δ
α-factor
i
ZST
norm. peak intensity
untreated
vehicle
10μM
20μM
30μM
40μM
50μM
ste2Δ
α-factor

Figure 3

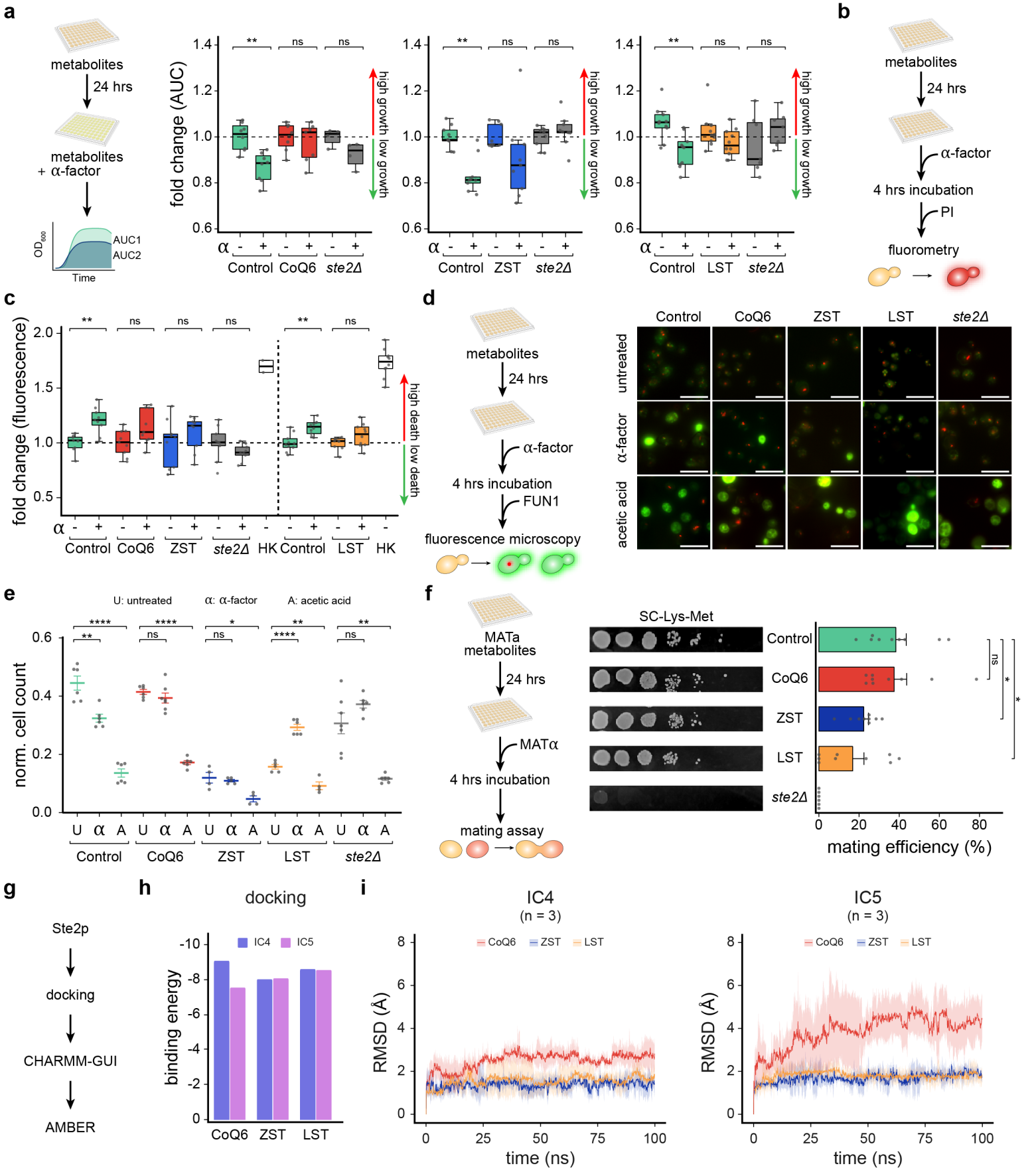
a
metabolites
24 hrs
metabolites
+ α-factor
OD600
AUC1
AUC2
Time
fold change (AUC)
high growth low growth
Control CoQ6 ste2Δ
Control ZST ste2Δ
Control LST ste2Δ
b
metabolites
24 hrs
α-factor
4 hrs incubation
PI
fluorometry
c
fold change (fluorescence)
high death low death
Control CoQ6 ZST ste2Δ HK Control LST HK
d
metabolites
24 hrs
α-factor
4 hrs incubation
FUN1
fluorescence microscopy
Control CoQ6 ZST LST ste2Δ
untreated
α-factor
acetic acid
e
U: untreated
α: α-factor
A: acetic acid
norm. cell count
Control CoQ6 ZST LST ste2Δ
f
MATa
metabolites
24 hrs
MATα
4 hrs incubation
mating assay
SC-Lys-Met
Control
CoQ6
ZST
LST
ste2Δ
mating efficiency (%)
g
Ste2p
docking
CHARMM-GUI
AMBER
h
docking
IC4
IC5
binding energy
CoQ6 ZST LST
i
IC4
(n = 3)
IC5
(n = 3)
CoQ6 ZST LST
RMSD (Å)
time (ns)

Figure 4

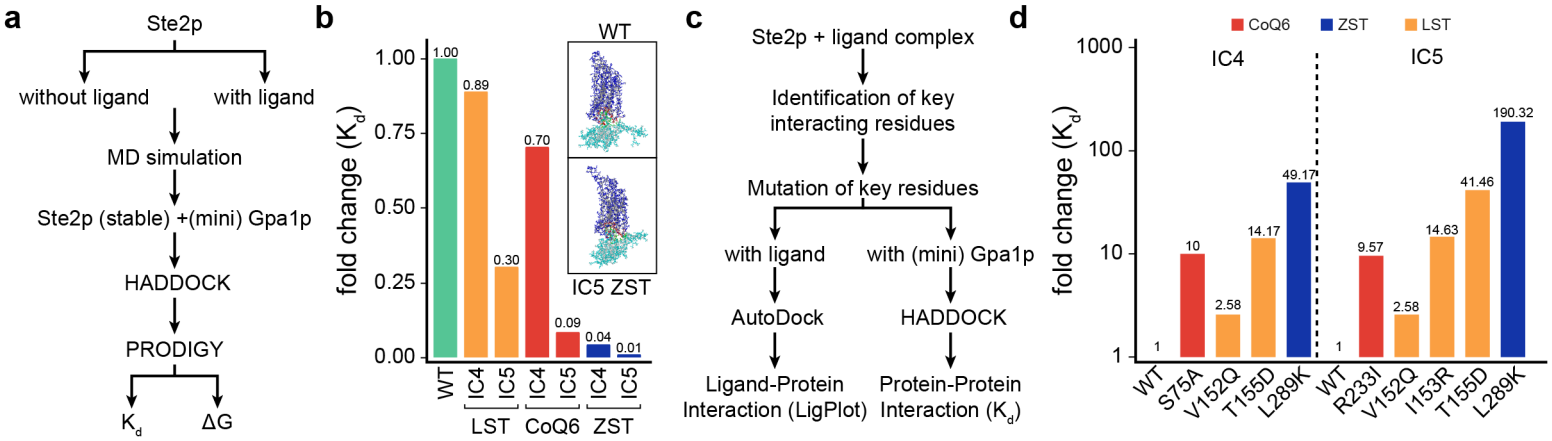

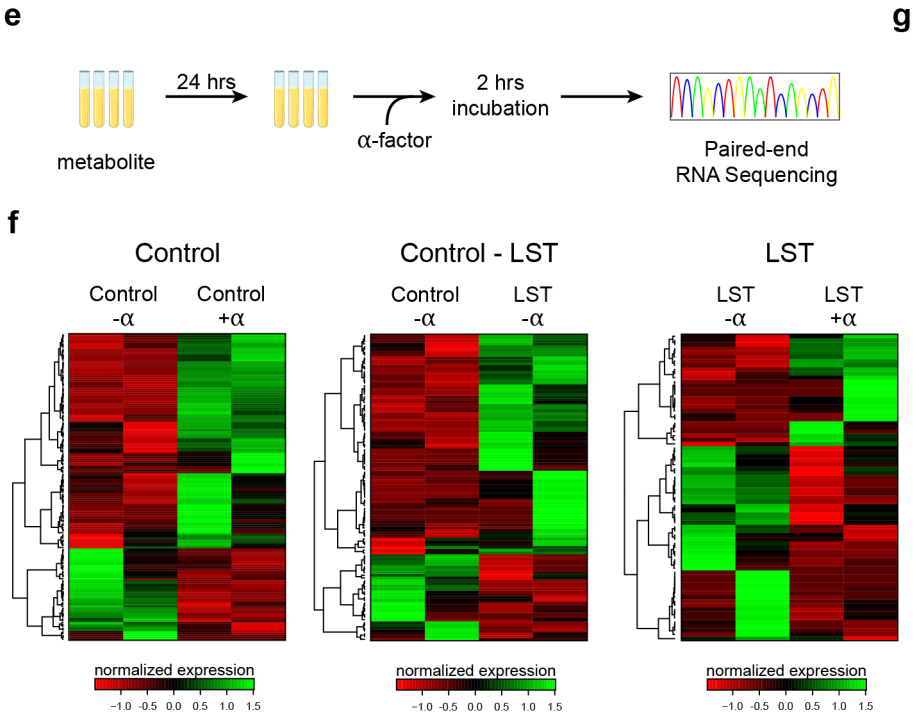

g

ORF	Gene	Control	Control - LST	LST	Mating	Apoptosis
YCL067C	*HMLALPHA2*	↑	↑	-	✓	✗
YCR040W	*HMLALPHA1*	-	↑	-	✓	✗
YDL045W-A	*MRP10*	-	↓	-	✓	✗
YDL075W	*RPL31A*	↓	-	-	✓	✗
YDR382W	*RPP2B*	↓	-	-	✓	✗
YDR461W	*MFA1*	-	↑	-	✓	✗
YKL180W	*RPL17A*	↓	-	-	✓	✗
YLR325C	*RPL38*	-	↑	-	✓	✗
YMR242C		↓	-	-	✓	✗
YNL145W	*MFA2*	↑	-	-	✓	✗
YPR159C-A		-	-	↑	✓	✗
YLR011W	*LOT6*	↓	-	-	✗	✓
YLR075W	*RPL10*	↓	-	-	✗	✓
YLR185W	*RPL37A*	↓	↓	-	✗	✓
YNL134C		↑	-	-	✗	✓
YPR133W-A	*TOM5*	-	-	↓	✗	✓

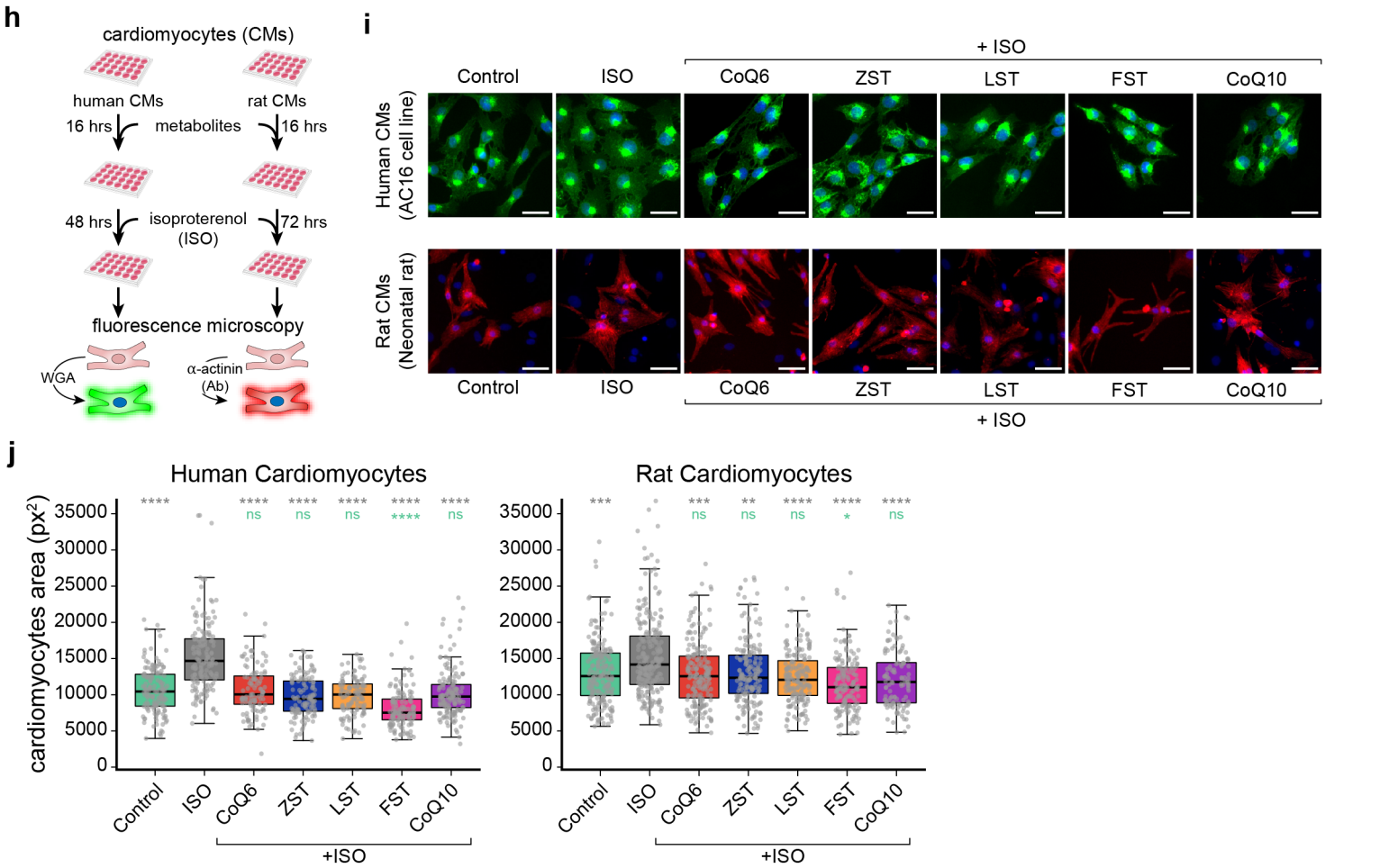

Figure 5